KeAi

CHINESE ROOTS
GLOBAL IMPACT

Contents lists available at ScienceDirect

Petroleum Science

journal homepage: www.keaipublishing.com/en/journals/petroleum-science



Original Paper

Shale weak cementation model and elastic modulus prediction based on nanoindentation experiment



Jian-Bo Wang ^a, Yang-Yang Zhang ^b, Jian-Tong Liu ^{a, *}, Xiao-Di Li ^{a, c}, Bo Zhou ^b, Yuan-Kai Zhang ^b, Bao-Xing Liang ^b

- ^a School of Petroleum, China University of Petroleum-Beijing at Karamay, Karamay, 834000, Xinjiang, China
- ^b China National Petroleum Corp Xinjiang Oil Field, Karamay, 834000, Xinjiang, China
- ^c Unconventional Petroleum Research Institute, China University of Petroleum-Beijing, Beijing, 102249, China

ARTICLE INFO

Article history: Received 26 November 2023 Received in revised form 28 March 2025 Accepted 28 March 2025 Available online 29 March 2025

Edited by Yan-Hua Sun

Keywords:
Shale
Nanoindentation
Multiscale
Weak cementation model
Flastic modulus

ABSTRACT

The successful development of shale oil and gas reservoirs is the biggest technological revolution in the oil and gas industry. Its key technologies are horizontal well drilling and fracturing, which are based on understanding the mechanical properties of reservoir rocks. Therefore, it is critical to obtain the reservoir mechanical parameters quickly, efficiently, and inexpensively. In this study, shale samples were collected from three basins in Southwest China, and the elastic modulus of shale in the indentation depth range of 0-5000 nm was obtained by nanoindentation experiments. Experimental results showed that different indentation depths had different physical characteristics. The shallower depths had the mechanical properties of single minerals, while the deeper depths had the mechanical properties of a multi-mineral composite. The difference between the two represented the cementation strength between the mineral particles. The error between the calculation results of the existing equivalent medium theoretical model and experimental data reached 324%. In this study, a weak cementation model was adopted, and three parameters obtained by nanoindentation experiments were considered: the soft component volume content, intergranular cementation strength, and mineral particle size. This solved the problem of assuming rather than calculating the values of some parameters in the existing model and realized the prediction of the macroscopic mechanical parameters of shale. The calculation error was reduced to less than 20%, and the test method and calculation model can be popularized and applied in engineering. © 2025 The Authors. Publishing services by Elsevier B.V. on behalf of KeAi Communications Co. Ltd. This is an open access article under the CC BY-NC-ND license (http://creativecommons.org/licenses/by-nc-nd/ 4.0/).

1. Introduction

At present, the recoverable volume of conventional oil and gas resources in the world is decreasing, while the demand for oil and gas resources is increasing. Unconventional natural gas accounts for an increasing proportion of the energy supply, and shale gas occupies an important position in the unconventional natural gas resources (Curtis, 2002; Jenkins and Boyer, 2008; Jiang et al., 2007). The development of shale gas in China has achieved great success, and the marine shale of the Longmaxi Formation has huge development potential in particular (Ma et al., 2021a). The key technologies for the successful development of shale oil and gas are horizontal wells and hydraulic fracturing. During development, it is

necessary to accurately obtain the mechanical parameters (Fisher et al., 2004; King, 2010; Martineau, 2007; Matthews et al., 2007; Olson, 2008; Warpinski et al., 2009). The rock elastic modulus is critical, especially in the compressibility evaluation of shale reservoirs (Britt and Schoeffler, 2009; Cipolla et al., 2008; Goktan and Gunes, 2005; Guo et al., 2015; Nejad et al., 2013; Rybacki et al., 2016). However, it is very time-consuming and labor-intensive to carry out rock uniaxial compression experiments on shale cores to determine the mechanical parameters, which increases construction costs and time (Grieser and Bray, 2007; Mullen et al., 2007; Rickman et al., 2008; Ye et al., 2020). The nanoindentation test method has been widely used in the development of shale oil and gas, which has promoted the progress of the unconventional oil and gas industry. Through a nanoindentation test, rock mechanical parameters such as the elastic modulus, hardness, and fracture toughness of shale reservoirs can be obtained and the creep behavior of shale can also be analyzed (Deirieh et al., 2012; Faghihi

E-mail address: ardow100@163.com (J.-T. Liu).

^{*} Corresponding author.

and Voyiadjis, 2012; Kabir et al., 2017; Kumar, 2012; Mighani et al., 2019; Shukla et al., 2013; Zargari et al., 2011).

In recent years, the nanoindentation test method has been adopted by many scholars to evaluate the mechanical properties of shale reservoirs (Bobko and Ulm, 2008; Kenechukwu et al., 2010; Ortega et al., 2007, 2009; Shukla et al., 2013; Ulm and Abousleiman. 2006; Ulm et al., 2007). The nanoindentation test method emerged in 1992 and is used to determine the mechanical characteristics of various materials, such as alloys, coatings, rocks, and concrete (Balko et al., 2017; Bei et al., 2005; Do et al., 2014b; Landman et al., 1990; Li et al., 2003; Ma et al., 2021b; Minor et al., 2006; Oliver and Pharr, 1992; Pătru et al., 2015; Sato et al., 2020; Shukla et al., 2015; Sun et al., 2020; Zhu et al., 2007). The application of the nanoindentation test method to shale has great advantages, as it can provide both elastic modulus and hardness data from a single test. In addition, the nanoindentation test method can be applied to samples of various sizes and shapes. For example, cuttings (about 1–5 mm) in the drilling process can be tested after being fixed with epoxy resin. In routine rock mechanics experiments, the sample size is a cylinder with a diameter of 1-2 inches and a height of twice the diameter (Carreño et al., 2018; Liu et al., 2016; Liu, 2015; Veytskin et al., 2017; Xiang et al., 2017; Yang et al., 2016, 2017). This feature greatly expands the number of test samples and reduces the time and cost of drilling cores (Yoon et al., 2019).

Scholars have carried out a large number of experimental studies of the mechanical properties of shale in different areas (e.g., Woodford, Barnett, Haynesville, Eagle Ford, and Lower Saxony Basin in North America) (Li et al., 2019; Liu et al., 2023; Luo et al., 2020; Yoon et al., 2019) and in different formations (e.g., the southern marine Longmaxi Formation, Zhangjiakou Xiamaling Formation, Bohai Basin, and Shahejie Formation in China) (Fan et al., 2019; Liu et al., 2020; Sheng et al., 2022; Wang et al., 2022a, 2022b; Zhao et al., 2020). These studies found that the elastic modulus and hardness of shale decreased with the increases in the clay content, organic matter content, and porosity (Khatibi et al., 2018; Kumar et al., 2012a, 2012b, 2015; Shukla et al., 2013; Zargari et al., 2011). Clay, organic matter, and pores contribute to a lower strength (or lack of strength) in shale, and thus, the increase in these content leads to a decrease in the rock strength (Kohli and Zoback, 2013; Sone and Zoback, 2013a, 2013b; Tembe et al., 2010; Wang et al., 2019). This finding is consistent with the research conclusions in various rock physics.

With the development of the nanoindentation test method, a test method called the continuous stiffness method has become highly regarded because it can analyze the elastic modulus at different indentation depths (Kenechukwu et al., 2010; Liu et al., 2016; Luo et al., 2021; Sheng et al., 2022; Wu et al., 2020; Xiang et al., 2017). As the indentation (intrusion) depth increases, this method can reflect the small-scale information of single minerals in shale and can also reflect the large-scale information at greater depths (Luo et al., 2021; Sheng et al., 2022). Therefore, nanoindentation is often used to study multiscale mechanical problems. It is expected that in the future, nanoindentation testing will be used to predict the macroscopic mechanical parameters of reservoirs in oil and gas production to improve the work efficiency (Fan et al., 2019). Our goal is to analyze the mechanical information of a single mineral in the rock when the indentation depth is small, to analyze the macroscopic mechanical behavior of multiple minerals when the indentation depth is large, and to build a model based on these two scales (Auvray et al., 2017; Li and Sakhaee-Pour, 2016; Luo et al., 2021; Veytskin et al., 2017; Zhang et al., 2017).

To predict the macroscopic mechanical parameters of shale, scholars have established a large number of models to solve this problem, such as the Voigt model, Reuss model, Hill model, Hashin—Shtrikman, and other average models. These types of

models use the volume ratio of components and the mechanical properties of each component as input parameters to predict the mechanical parameters of the rock as a whole (Herrmann et al., 2018; Hu et al., 2013; Liu and Fu, 2020; Nezhad et al., 2016; Nhabanga et al., 2021; Qian et al., 2020; Sone and Zoback, 2013a, 2013b). The prediction result is a range, often given in the form of upper and lower limits, and the accuracy needs to be improved. Another class of methods considers stress and strain interactions between components to predict macroscopic mechanical behavior, such as Eshelby's equivalent inclusion theory (Eshelby, 1957), the self-consistent method (Zimmerman, 1984), the Mori-Tanaka method (Gommers et al., 1998), the generalized self-consistent method, and the differential method. Compared with the former class of methods, it has certain value in engineering applications (Giraud et al., 2007; Li et al., 2022; Mavko et al., 2009; Vasin et al., 2013; Wang et al., 2021; Yin et al., 2020; Zhao et al., 2019). Another method is widely used in the prediction of elastic modulus and hardness of shale, that is, the packing density method, but the predicted value of this kind of calculation is generally higher than that of experimental test (Abedi et al., 2016). In addition, the calculation parameters in this type of methods are very complicated, and a large number of parameters cannot be obtained through actual tests. In the prediction of shale macroscopic mechanical parameters, these methods require assuming some microscopic mechanical parameters before calculation, making their application in engineering extremely difficult.

Therefore, in this study, a new method was constructed based on the nanoindentation test data to solve the problem of predicting the macroscopic mechanical parameters of shale. First, through the continuous stiffness method in the nanoindentation test, the mechanical parameters of shale at different indentation depths were tested. Then, the mechanical parameters of a single mineral and the mineral average in shale were analyzed and obtained. Based on these parameters, the cementation strength between the minerals in shale was calculated. Finally, these parameters were substituted into the model to verify the fit between the predictions and experimental data.

2. Materials and methods

2.1. Sample information

The samples collected in this study came from three basins in China: Fuling Longmaxi and Qianjiang Longmaxi from the Sichuan Basin, Songyuna Nenjang from the Songliao Basin, and the Yan'an Yanchang from the Ordos Basin (Gao and Hu, 2018). The shale of the Upper Ordovician Wufeng Formation and Lower Triassic Longmaxi Formation in the Sichuan Basin is the main production layer of shale gas in China. The Longmaxi Formation shale collected in this study (Fuling Longmaxi, Qianjiang Longmaxi) came from the Fuling and Qianjiang areas of Chongqing (Tang et al., 2019; Wang et al., 2017; Ma and Xie, 2018; Zhao et al., 2018). The development of shale oil in the Upper Cretaceous Nenjiang Formation in the Songliao Basin is still in its preliminary stage, but it has great development potential. In this experiment, one shale sample (Songyuan Nenjiang) was collected from the Nenjiang Formation in the Songyuan area of Jilin Province. The shale of the Upper Triassic Yanchang Formation in the Ordos Basin is the main production layer for continental shale oil development in China. In this study, samples (Yan'an Yanchang) were collected from the 7th Member of the Yanchang Formation in Yan'an, Shaanxi Province (Gao and Hu, 2018; Xiong et al., 2016).

The mineral composition of shale was determined by X-ray diffraction (XRD), and the mineral identification accuracy of the test was one decimal place. The test of the total organic carbon (TOC)

content was completed using a Leco CS230 carbon/sulfur analyzer, and its test accuracy was 0.5% (Zhao et al., 2018). Since both clay and organic carbon are soft components in shale, they have a great influence on micromechanical properties. Therefore, by substituting the TOC content into the mineral composition percentage obtained by the XRD analysis, we obtained the composition results shown in Table 1. It can be observed that the total clay and organic matter content of the collected shale ranged from 19.7% to 58.1%. The other main components were quartz, feldspar, calcite, dolomite, and pyrite, which are relatively hard minerals. Fig. 1 shows scanning electron microscopy (SEM) images of shale samples, and the equipment used was a desktop electron microscope TM3030 from Hitachi, Japan. From the microscopic images, the grain size of the minerals, such as quartz, feldspar, and calcite contained in the shale, was determined to be approximately 2–31 μ m.

2.2. Laboratory equipment

The equipment used in the indentation test experiment was a Keysight Technologies G200 nanoindenter (as shown in Fig. 2(a)). Fig. 2(b) shows the rigidity of the instrument frame was \geq 5×10^6 N/m. The load test range was 0–500 mN, and the resolution was 50 nN. The vertical displacement range was 0–500 μm, and the resolution was 0.01 nm. The indenter used was a Berkovich diamond indenter, whose top radius of curvature could reach 20 nm. A smaller radius of curvature corresponds to a sharper indenter, which will obtain more reliable mechanical parameters at shallower indentation depths. The conventional static nanoindentation test method can obtain parameters such as the material load, indentation depth, time, hardness, elastic modulus, and fracture toughness. In addition, continuous stiffness measurement (CSM) can be performed to expand the method of dynamic indentation on the basis of conventional static indentation. During the test, the hardness, elastic modulus, loading, contact stiffness, and contact area curves could be displayed in real time along with the indentation depth. The frequency of the dynamic press-in simple harmonic force of the device was 1-300 Hz, and the amplitude was from 0.1 µN to 4.5 mN. This method of continuous mechanical parameter testing can obtain mechanical parameters at different depths in one test, without considering the scale effect caused by the differences in mineral particles at the test site. Using these parameters to analyze the mechanical parameters of shale at different scales is an effective research method for describing the cross scale mechanical properties of rocks.

2.3. Experimental procedure

The nanoindentation experiment in this study included four steps: sample preparation, nanoindentation testing, observation of indentation features, and data analysis. These are described below.

Step 1. Since the shale samples were easily broken in the cutting process, they needed to be fixed. First, the sample was cut into a disc shape with a thickness of 20 mm and a diameter of 20 mm. Then, the sample was placed in a circular mold, which was filled with epoxy. After the epoxy hardened, the sample could be fixed and wrapped. Again, the shale encased in epoxy was revealed by sanding. Finally, 3000-grit sandpaper was used to polish the surface of the sample to make it smooth and clean, and then it was polished with flannelette. The polished sample was put into a drying oven at $100\,^{\circ}\text{C}$ for 24 h, and the sample preparation was completed. The completed sample is shown in Fig. 3.

Step 2. The surface approach velocity used in the nanoindentation test was 30 nm/s, and the maximum strain rate target was 0.05. The CSM frequency target was 45 Hz, and the harmonic displacement target was 2 nm. The indentation depth limit was 5000 nm, and the loading limit was 800 mN. Each test included three parts: loading, holding, and unloading, and the holding time was 5 s. The indentation test is shown in Fig. 4. The indentation test interval was 0.8 mm, which was a 5×5 dot matrix, and each sample had a total of 25 tests. From the morphology of the indentation surface shown in Fig. 4(c), it can be observed that the deformation of the indentation surface is isolated from each other, and each indentation test will not affect each other. A spacing of 0.8 mm between the indentations is appropriate. During the experiment, the indentation depth, load, elastic modulus, and hardness data were recorded. According to the indentation after the nanoindentation test in Fig. 4, it can be seen that there is no connection between the bulge and deformation at the edge of the indentation. Based on this image, we can confirm that there is no impact between indentations. In addition, according to the "one-tenth rule" criterion of nanoindentation, it is generally believed that the influence of the indentation is ten times the cross section of the indentation. As shown in Fig. 1, the radius of indentation is 0.03 mm, which is 0.3 mm when multiplied by 10 times, which is much smaller than the indentation distance of 0.8 mm in the experiment, indicating that this experimental design is reliable. Step 3. The residual indentation after the test was observed with a Japanese Hitachi desktop TM3030 electron microscope, and

Table 1Mineral composition and porosity data of shale samples.

Sample No.	Formation	Mineral composition, %						TOC content, %	Clay + TOC content, %	Porosity, %
		Quartz	Feldspar	Calcite	Dolomite	Pyrite	Clay			
F1	Fuling Longmaxi	50.8	7.6	3.6	11.7	5.1	18.3	2.9	21.3	6.18
F2		51.0	6.5	5.4	9.9	3.8	17.6	5.9	23.5	5.04
F3		53.9	4.2	3.2	8.4	5.7	20.7	4.0	24.7	4.09
F4		47.9	6.2	2.9	8.3	5.1	24.4	5.3	29.6	3.62
F5		36.6	10.7	9.1	6.0	5.9	30.5	1.2	31.7	5.92
F6		36.7	7.7	7.5	5.1	7.8	32.3	2.9	35.3	6.09
Q1	Qianjiang Longmaxi	41.4	4.6	25.2	7.3	1.9	18.4	1.3	19.6	4.19
Q2		47.1	6.7	6.3	7.8	3.1	27.6	1.4	29.0	7.25
Q3		37.4	5.1	9.5	5.3	0	34.3	8.3	42.6	3.86
J1	Songyuan Nenjiang	17.3	13.0	6.0	4.0	16.5	41.4	1.8	43.2	5.08
J2		18.0	12.1	5.7	3.6	2.5	57.3	0.8	58.1	4.37
J3		20.5	12.7	6.7	6.1	2.7	50.0	1.3	51.3	4.83
J4		18.6	12.3	4.5	5.9	0.9	56.6	1.2	57.8	5.10
Y1	Yan'an Yanchang	43.9	5.2	4.2	0	4.9	39.2	2.8	42.0	4.59
Y2		27.5	8.1	0.6	7.5	4.9	47.6	3.8	51.4	6.64

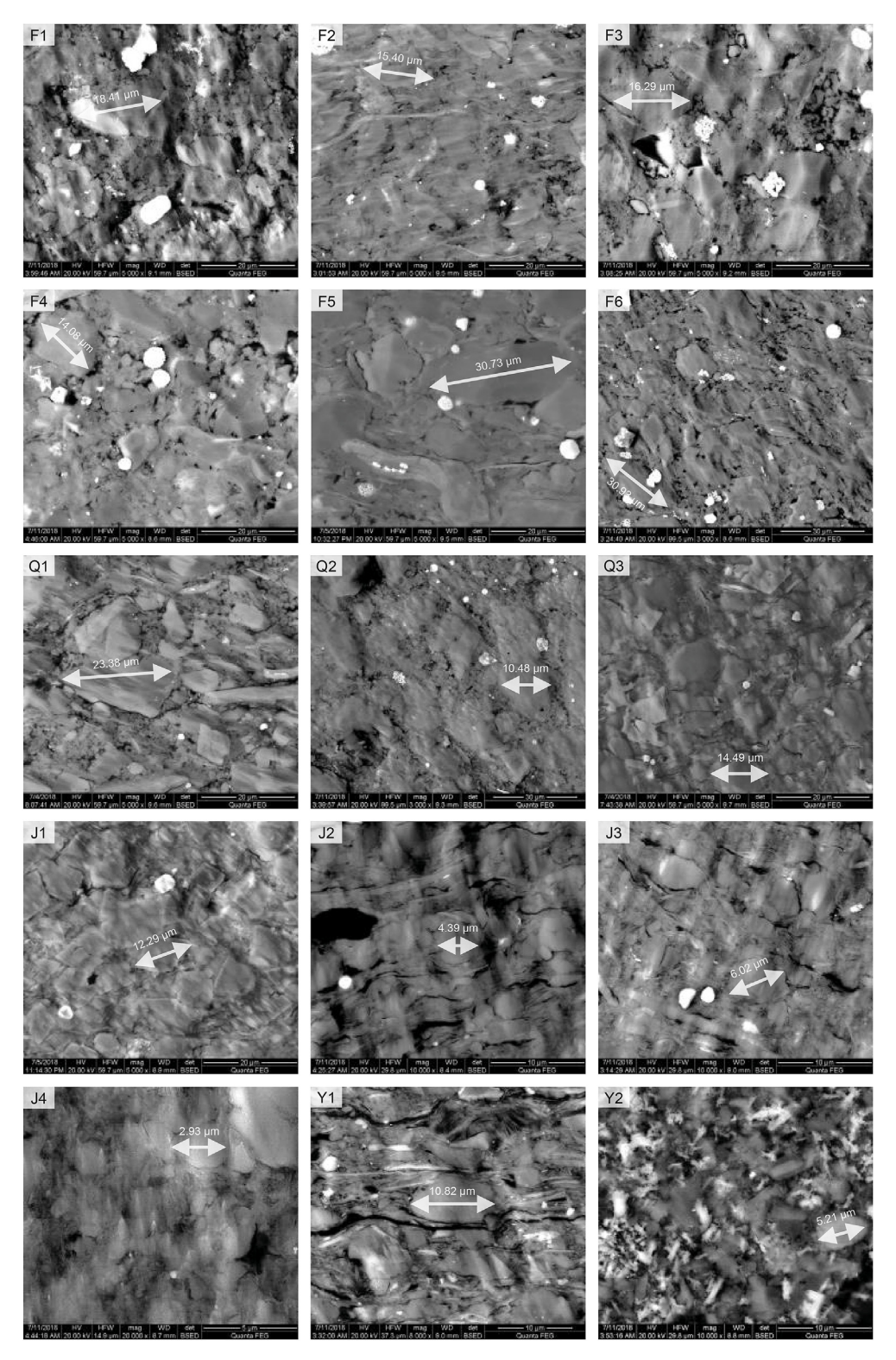


Fig. 1. SEM images and mineral particle size analysis of experimental samples.

the corresponding relationship between the mechanical parameters and the indentation was obtained by analyzing the continuous stiffness test method.

Step 4. The different indentation depths during nanoindentation were analyzed to determine the mechanical properties at different scales in the rock.

3. Results and analysis

3.1. Indentation depth-load curve

Fig. 5 shows the indentation depth—load curves obtained by the continuous stiffness method. It can be observed that the

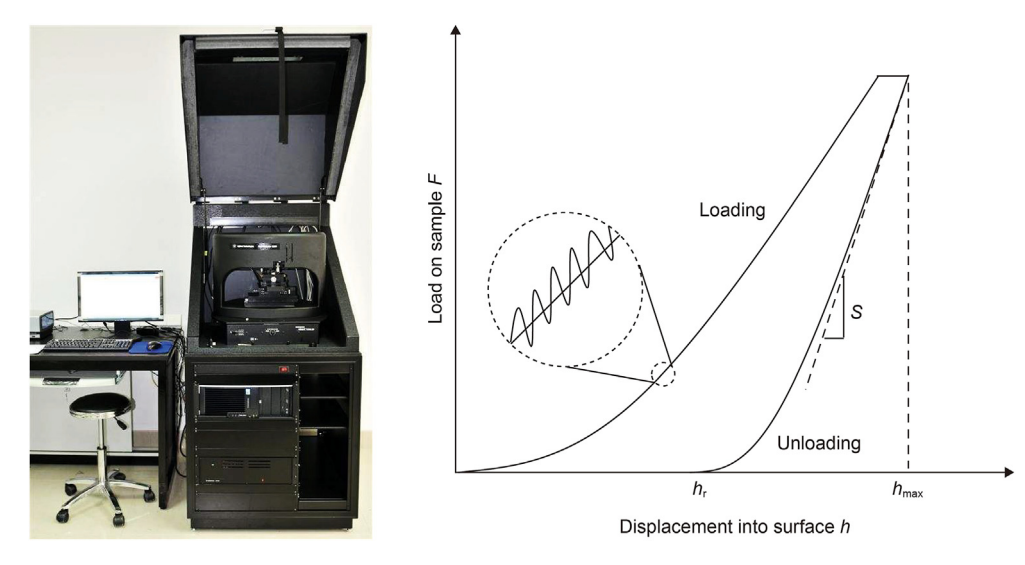


Fig. 2. Schematic diagram of experimental equipment and loading.

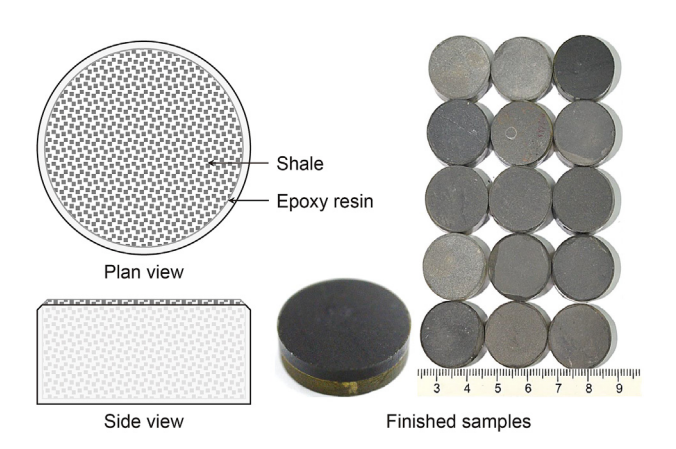


Fig. 3. Photos of the experimental sample production process and sample photos.

indentation depth-load curves of different shale samples were different, reflecting the differences in their mechanical properties. When the indentation depth was large and the load was small, it indicated that the shale had a low strength. In contrast, a smaller indentation depth and a larger load indicated that the shale had a higher strength. During the experiment, the indentation depth was designed to be 5000 nm, and the load limit value was 800 mN. However, not all sample indentation tests met this condition in the experiment, which was related to the mechanical properties of the sample. As shown in Fig. 6, the indentation depth and load curves of the different group samples. From Table 1, it can be seen that the clay and organic matter contents of F1, F5, J1, and J4 were 21.3%, 31.7%, 43.2%, and 52.2%, respectively. With the increase in the clay and organic matter content, under the same indentation depth, the load became smaller. As the content of clay and organic matter decreased, the indentation depth became smaller under the same load conditions.

According to the loading and unloading curve diagram of indentation test shown in Fig. 2, multiple cyclic loads are used in the loading process to obtain loading and unloading curves of different pressing depths (shown in the circular dotted line in Fig. 2). These curves can be calculated to obtain the slope of the unloading part as shown in Fig. 2, which is the contact stiffness *S*. According to the Oliver—Pharr method, two mechanical properties

of the impingement modulus E_t at the indentation position of the measured material can be calculated from the curve shown in Fig. 5 by applying the mechanical model:

$$E_{\rm t} = \frac{\sqrt{\pi}S}{2\beta\sqrt{A_{\rm c}}}\tag{1}$$

where F is the maximum load value on each cyclic loading and unloading cycle curve; A_c is the contact area between the indenter and the sample, A_c can be estimated by the following equation: $A_c = 24.56h_{\text{max}}^2$; S is the contact stiffness, $S = \frac{dP}{dh}\Big|_{h_{\text{max}}}$; β is the coefficient of head correction ($\beta = 1.034$); h_{max} is the vertical distance from the tip of the indenter to the contact point between the indenter and the sample.

The elastic modulus E can be calculated by the following relationship:

$$\frac{1}{E} = \frac{1 - \mu_{\rm t}^2}{E_{\rm t}} + \frac{1 - \mu_{\rm i}^2}{E_{\rm i}} \tag{2}$$

where μ_t is the Poisson's ratio of the test material 0.25; E_t is the elastic modulus of the indenter, $E_t = 1141$ GPa; μ_i is the Poisson's ratio of the head 0.07.

Fig. 7 shows the elastic modulus calculated according to the curve in Fig. 5. Each curve represents the mechanical parameters obtained from the dynamic indentation test based on the continuous stiffness method as the indenter pressed into the sample. These results represent the local mechanical properties of the surface at different indentation depths and different indentation areas. Fig. 8 shows the indentation depth-load curves and elastic modulus curves corresponding to four indentation tests of sample F2. It can be observed that as the indentation depth increased, the four curves tended to a certain fixed value after reaching the indentation depth of 3000 nm, and they were relatively close. In Fig. 8, the blue and red elastic modulus results showed that they rapidly increased to the peak values as the indentation depth increased, then they decreased, and finally, they tended to a fixed value. However, there was a difference between the two peaks, which was related to the mineral composition at the indentation position. The green curve shows that the elastic modulus increased rapidly with indentation depth and then tended to a stable value. In the purple curve, the elastic modulus increased slowly to a fixed

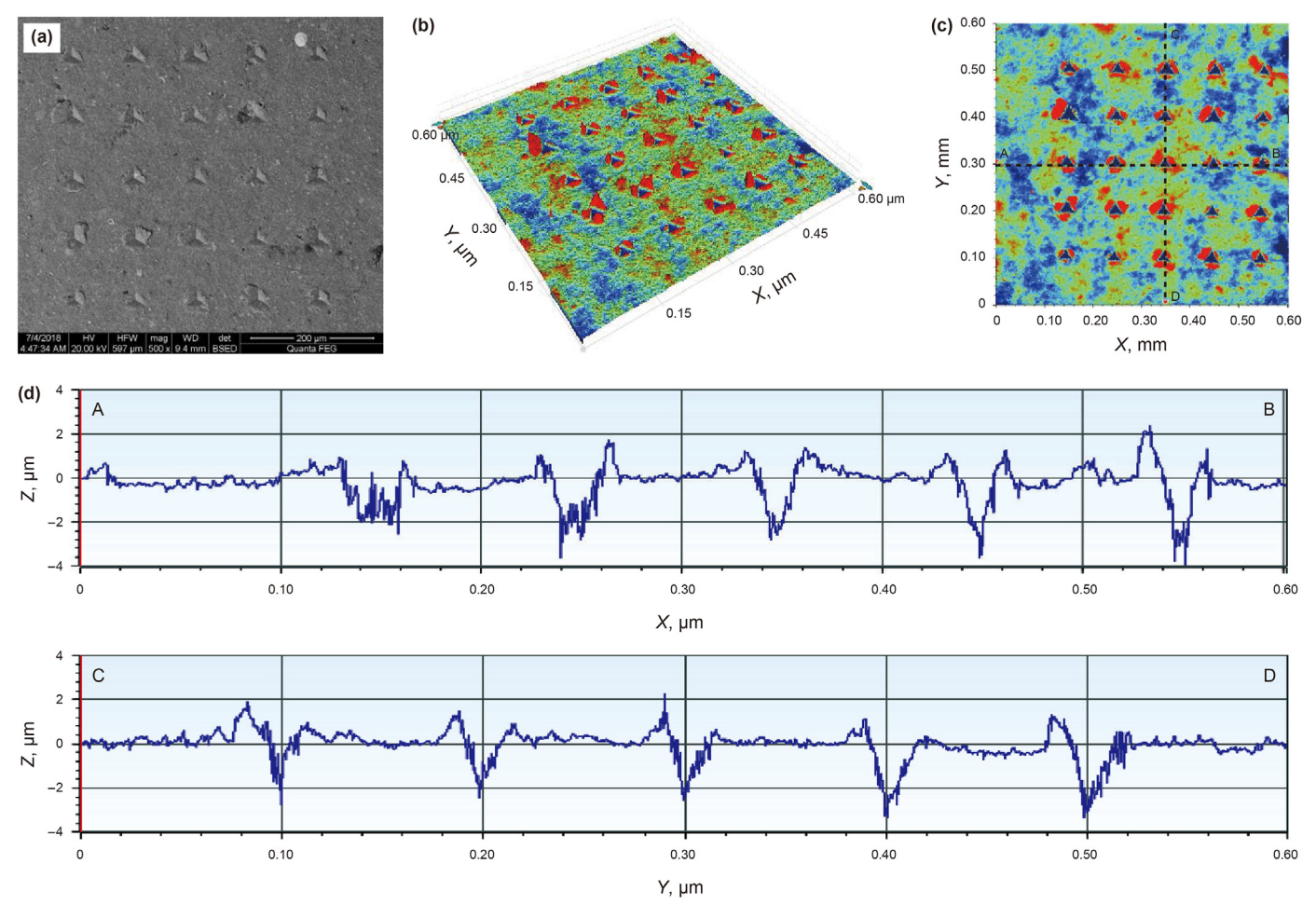


Fig. 4. Surface morphology after indentation testing. (a) SEM images after experiment; (b) Three-dimensional surface morphology of the indentation; (c) Two-dimensional surface morphology of the indentation; (d) Morphology data corresponding to the AB and CD lines in Fig. 4(c).

value as the indentation depth increased. In particular, the red curve showed a pop-in phenomenon at the indentation depth of 2407.48 nm. Based on previous research, the pop-in phenomenon was related to the fracturing of surface minerals (Luo et al., 2021; Sheng et al., 2022).

3.2. Nanoindentation morphology and mineral distribution characteristics

The test scheme used in the experiment was a 5×5 dot matrix, and the overall shape of the indentation of each sample is shown in Fig. 9. In order to correspond to the indentation data and the indentation point, a mark was made near the first indentation point. Representative indentation data was selected for each group of samples, and the corresponding relationship between the elastic modulus of each mineral, and then the indentation process was analyzed, as shown in Fig. 11.

Based on the SEM and energy-dispersive X-ray spectroscopy (EDS) images (Fig. 10), the mineral composition at the indentation point was determined. The components of samples F1-10 and Q1-09 were organic matter in the initial press-in area, and their corresponding elastic moduli were 10.25 and 14.43 GPa, respectively. F4-06 and Q2-12 were calcite, and their corresponding elastic moduli were 69.73 and 78.09 GPa, respectively. The corresponding minerals of F5-08 and F5-18 were quartz when they were initially indented, and their elastic moduli were 90.51 and 81.97 GPa, respectively. The corresponding minerals of Q1-01 and Q3-11 were

feldspar at the initial indentation, and their elastic moduli were 51.24 and 41.99 GPa, respectively. Y1-03 and Y1-12 were clays, and their corresponding elastic moduli were 19.60 and 18.87 GPa, respectively. The corresponding minerals of F2-13 and F6-06 were pyrite during the initial indentation, and the elastic moduli were 172.75 and 194.87 GPa, respectively. The data from this analysis shown in Figs. 7 and 8 reflect the results at different depths. The mechanical parameters were those of the single-phase minerals at the initial indentation, and they were the overall mechanical parameters of the multiple minerals after the indentation depth was greater than 3000 nm.

As shown in Fig. 11, the area inside the dotted white circle was higher than the surrounding area. Due to the uneven surface, the indenter deflected after being pressed into the surface, resulting in high data values, which were excluded. As a result of the uneven surface, the experiment yielded abnormal data resulting in some data that were not valid.

4. Analysis and statistics of mechanical parameters of micron indentation

4.1. Analysis of rock mechanics behavior in indentation test

Through this experiment, the elastic modulus of shale at different indentation depths was obtained, as shown in Fig. 7. It can be seen from the above analysis that the elastic modulus was constantly changing with the indentation depth. In the shallower

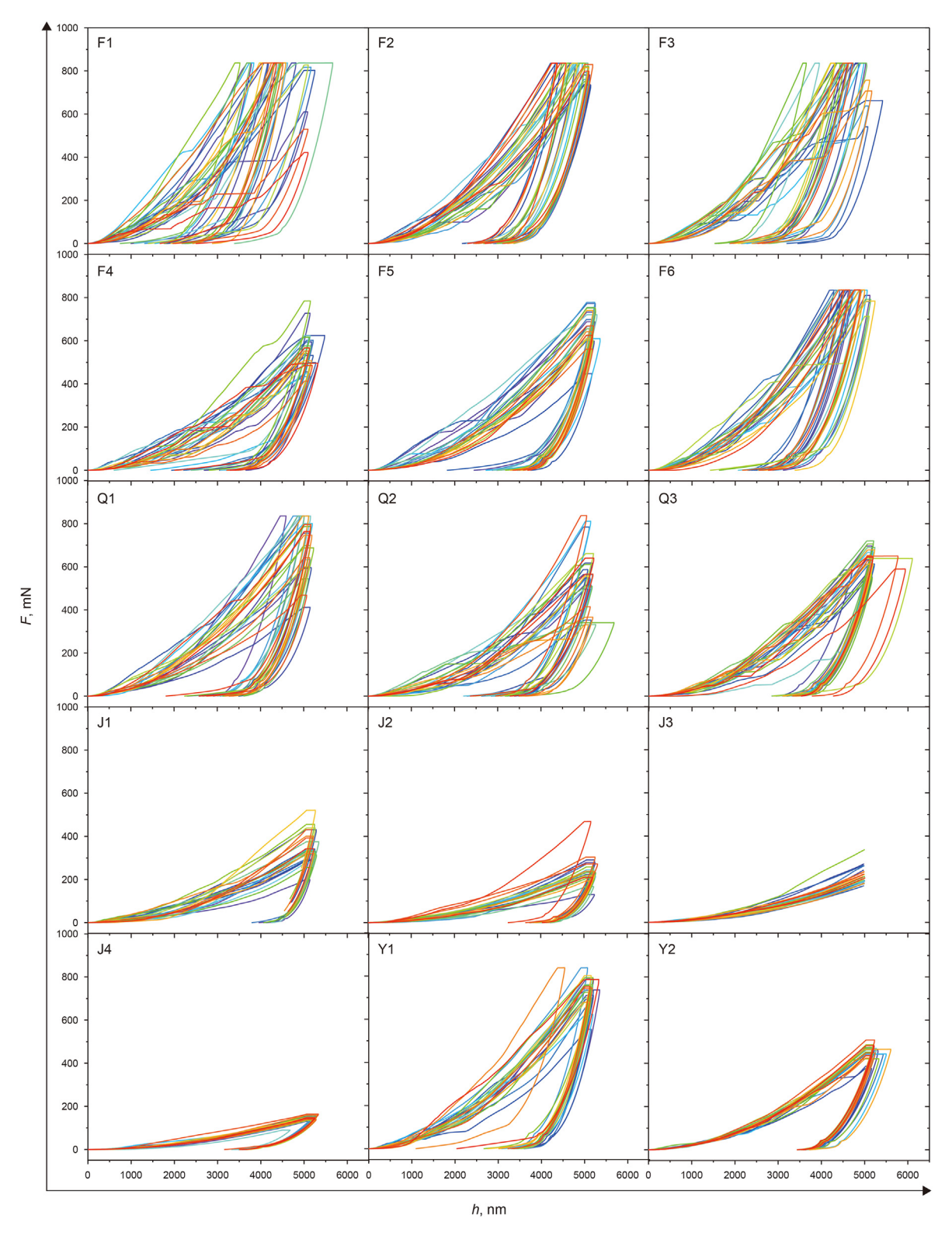


Fig. 5. Indentation depth vs. load curves of each group of samples.

depth range (such as depths less than 500 nm), the elastic modulus was more discrete due to the influence of individual minerals at the indentation point. In a larger depth range (such as depths greater than 3000 nm), the indenter covered multiple mineral particles, and the elastic modulus was the homogenized value of multiple minerals. This homogenized value can be called a macroscopic mechanical parameter. Based on the analysis of Figs. 8 and 10, it can

be seen that as the indentation depth increased, the sample surface composition transitioned from a single mineral to multiple minerals, and the elastic modulus either changed from large to small or from small to large and finally converged to a certain constant value. These phenomena indicated that the numerical values at shallower indentation depths were related to a single mineral, while at larger depths, they were related to multiple minerals and

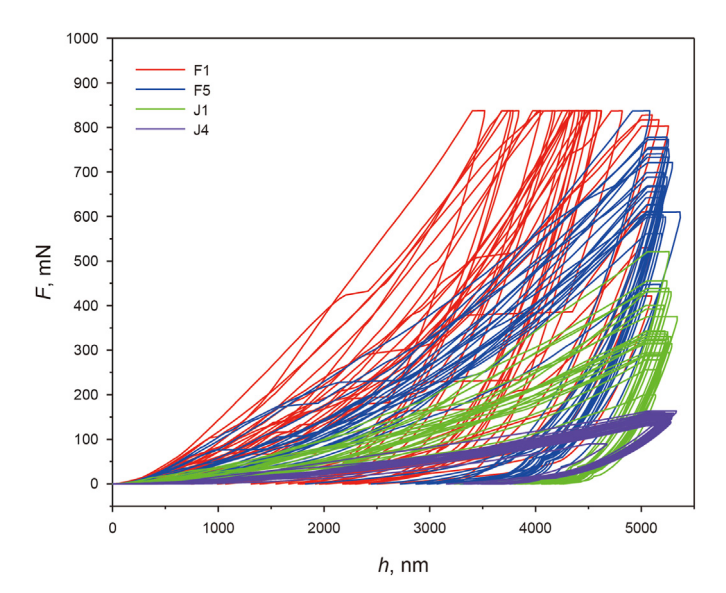


Fig. 6. Indentation depth vs. load curves of samples F1, F5, J1, and J4.

their interactions. Based on these analyses, the peaks within the depth range of 0–500 nm in the data shown in Fig. 7 corresponded to the microscopic mechanical parameters of the single minerals, and the peaks within the depth of 3000–4000 nm corresponded to the macroscopic mechanical parameters under the action of multiple minerals. The statistical results are shown in Fig. 12.

In order to intuitively explain the process in the press-in process, a schematic diagram is shown in Fig. 13. The components in shale were divided into two categories: hard components and soft components. The hard components consisted of quartz, feldspar, calcite, dolomite, and pyrite. When the indentation depth was relatively shallow, the indenter squeezed the hard minerals, and the minerals themselves deformed. The elastic modulus corresponded to the single-phase stage of the red curve shown in the right figure in Fig. 13, representing the mechanical characteristics of the mineral itself. When the indentation depth was further increased, the elastic modulus gradually decreased after the transition stage and finally tended to a constant value. This transitional stage represented the transition of the mechanical parameters from a single phase to multiple phases. Based on the testing principle of coating materials, we believe that the difference at this stage reflected the deformation difference between the hard components and the surrounding soft components, and thus, it could reflect the cementation strength (Do et al., 2014a; Pătru et al., 2015; Luo et al., 2021).

We define the difference between the single phase and multiple phases as ΔE , and we also performed the statistical analysis, as shown in Fig. 14. The particle size data in this figure is obtained according to the SEM image test shown in Fig. 1. Fig. 13 also shows the mechanical behavior of the soft components with the indentation depth. The soft components included clay, organic matter, and pores, and these were weaker components. When the indentation depth was relatively shallow, the indenter squeezed the soft components, causing them to deform. This corresponded to the single-phase stage of the blue dotted line on the right of Fig. 13, which represented the mechanical characteristics of the mineral itself. When the indentation depth was further increased, the elastic modulus gradually increased to a certain constant value, in contrast to the aforementioned hard components. However, due to the excessive deformation of the soft components, as the indentation depth increased, this stage represented the characteristics of continuous hardening of the soft components and could not reflect the mechanical characteristics of the cementation.

4.2. Analysis of main controlling factors of macroscopic elastic modulus

Based on the results above, we sought to establish the relationship between the single phase and multiple phases in order to predict the macroscopic mechanical parameters of shale through nano-indentation test data in future engineering projects. Based on the existing equivalent medium theory, the components in rocks are usually analyzed with the volume contents of hard components or soft components as variables. In order to convert the data in Table 1 into volume percentages, we needed to know the density of each component of shale. Based on the mineral densities calculated by Shukla et al. (2013), the volume percentages of each sample in this study were calculated. Furthermore, the relationship between the volume content of the soft components and the elastic modulus of indentation was obtained statistically. For comparison, we included the shale data of four blocks in Woodford, Barnett, Haynesville, and Eagle Ford (Li et al., 2019; Liu et al., 2023; Luo et al., 2020; Yoon et al., 2019; Shukla et al., 2013). As shown in Fig. 14, as the content of the soft components increased, the elastic modulus decreased, and this variation trend was relatively consistent in the different blocks (Sone and Zoback, 2013a, 2013b). We can see that the indentation elastic moduli of shale in the different blocks were quite different with the same content of soft components.

The content of soft components in shale is the key factor of its macroscopic mechanical parameters. As shown in Fig. 15, the volume contents of soft components in the test data of each sample group were fitted with the macroscopic elastic modulus values, and the correlation coefficient was 0.65. In order to study the influence of soft components on the elastic modulus, a large number of studies have used the method of bulk density and obtained good results (Abousleiman et al., 2010; Ortega et al., 2009; Ulm et al., 2007). In fact, the bulk density already reflects the volume content of the soft components in shale. Therefore, we did not consider it necessary to perform compacted density calculations. In addition, we also fitted the relationship between the macroscopic elastic modulus and the volume contents of soft components, the average value of ΔE , and mineral particle size, and we found that the correlation coefficient of ΔE reached 0.91, and the correlation coefficient of the mineral particle size was 0.62. These fitting results showed that the volume contents of soft components, the average value of ΔE , and the mineral particle size were the key factors affecting the macroscopic mechanical parameters.

5. Calculation of macroscopic elastic modulus based on nanoindentation data

5.1. Multiphase composite media model of ideal cementation surface

Predicting the macroscopic elastic modulus through nanoindentation is an important issue for engineering, as it means that the macroscopic mechanical parameters can be predicted using drilling cuttings. In order to compare the accuracies of these models for predicting the cross-scale mechanical parameters of shale, the mechanical parameters were calculated using the Voigt model, Reuss model, Hill model, and Hashin—Shtrikman model. The single-phase mechanical parameters used in these models were the test data from the experiment shown in Fig. 10, and the calculation results are shown in Fig. 16. It can be clearly seen that some macroscopic mechanical parameters calculated by the model were in good agreement with the experimental results. As shown in Table 2, the calculation error of sample Y1 through the

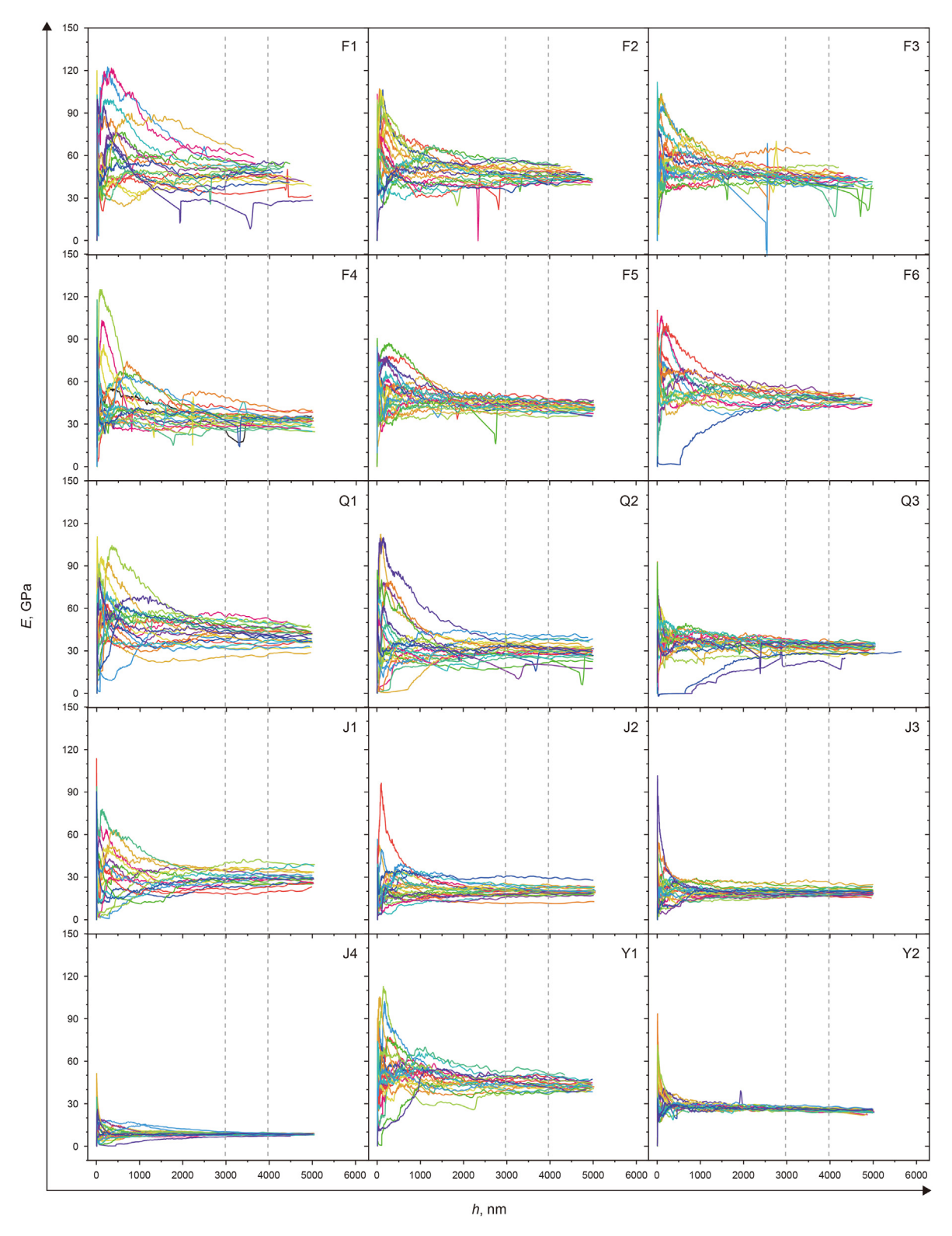
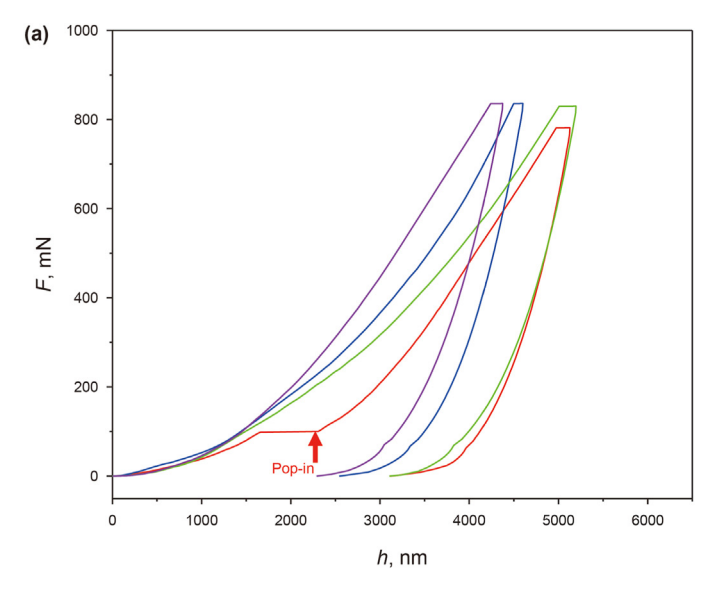


Fig. 7. Indentation depth vs. modulus curves of each group of samples.

Hashin—Shtrikman model reached a minimum of 2.36%. However, there were still some data with large differences from the model predictions. As shown in Table 2, the error reached 324.96%. Some experimental data were much smaller than the lower limit of the model calculation results (such as the Reuss model and Hashin—Shtrikman-model predictions). Most of the calculation

results had errors of more than 20%, which is an unacceptable result, and a more optimized model is needed to solve this problem.

To account for the interactions between components, the mean field method was used. In this analysis, the microscopic field in each component (phase), and the characteristic values of the stress and strain of each phase are replaced by corresponding average



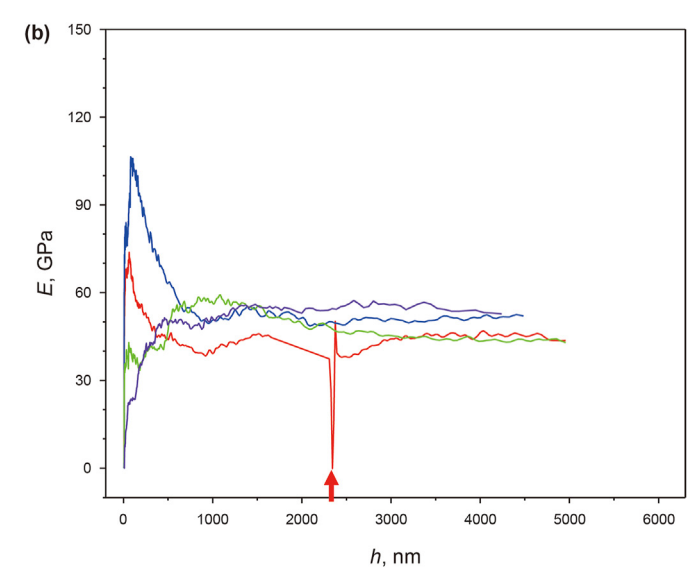


Fig. 8. Four indentation test results of sample F2. (a) Indentation depth vs. load curves; (b) Indentation depth vs. modulus curves.

values. Using the microscale topology, the morphology and distribution of the material microstructures are described by statistical information about the shape, orientation, and phase distribution of the inclusions. The relatively mature theories mainly include Eshelby's equivalent inclusion theory, the self-consistent method, the Mori—Tanaka method, the generalized self-consistent method, and the differential method. A variety of theoretical methods have been developed based on the study of composite reinforced materials, and this paper will focus on the application of the Mori—Tanaka method.

5.2. Multiphase composite media model considering weak cementation surfaces

We carefully analyzed the reasons that some of the results calculated by the above models deviated from the experimental results. These models are usually used to discuss the influence of the rock composition and porosity on the macroscopic modulus of rock. The models assume that the cementation surface between different components is an ideal interface, and its strength is not affected by different rocks. However, it can be seen from Fig. 15 that the mechanical property parameter ΔE of the cementation surface is closely related to the macroscopic elastic modulus. At the same time, the experimental results shown in Fig. 16 were generally smaller than the prediction results of the above models. These phenomena indicate that the cementation surface between the different rock components was not an ideal interface but a weak surface. When predicting macroscopic mechanical parameters based on nanoscale mechanical parameters, it is necessary to consider the role of weak cementation surfaces to improve the prediction accuracy.

Constraints to this study is a weak cementation surface resulting in a special form of a multiphase composite medium, which has important practical significance and wide application value in the design of composite microstructures. The mechanical properties of a weak cementation surface are closely related to the cement composition, compaction, and cementation in the rock formation process, and there are great differences between different rocks. The strength of a weak cementation surface is low, and it can easily undergo large deformation or cracking, which affects the macroscopic mechanical behavior of the composite medium. The microscopic morphology of a weak cementation surface is very complex,

and the thickness is small and difficult to measure accurately. If the surface were treated as a cementation surface with non-zero thickness, theoretical calculations and numerical analysis would be very difficult. Therefore, based on the material mechanics model of weak cementation surfaces (Benveniste, 1985; Hashin, 1991; Zhong and Meguid, 1997), the surface was simplified to a zero-thickness cementation surface, and the deformation of the weak cementation surface was equivalent to the displacement discontinuity on both sides of the cemented surface. This displacement discontinuity included shear slip and normal separation of the cemented surfaces.

5.2.1. Zero-thickness weak cementation surface model

The zero-thickness weak cementation surface model simplifies the cemented surface between the matrix and inclusions to a zerothickness cemented surface. The discontinuity of the displacement vector on both sides of the cemented surface was a linear function of the stress vector, and the expression is written as

$$\begin{cases} \left[\sigma_{ij}\right]n_{j} = 0\\ \left[\mu_{j}\right]\left(\delta_{ij} - n_{i}n_{j}\right) = \alpha\sigma_{kj}n_{j}(\delta_{ik} - n_{i}n_{k})\\ \left[\mu_{j}\right]n_{i}n_{j} = \beta\sigma_{kj}n_{k}n_{j}n_{i} \end{cases} \tag{3}$$

where $\mu_{\rm j}$ and $\sigma_{\rm ij}$ are the displacement and stress, respectively; $n_{\rm i}$ is the unit vector component of the external normal direction of the cemented surface; the amount of discontinuity $\left[\mu_{\rm j}\right]=$ outside value – inside value; α and β represent the flexibility of the tangent and normal directions of the cemented surface, respectively, ($\alpha \geq 0$ and $\beta \geq 0$); and $\delta_{\rm ij}$ is the symbol of Kronecker δ .

The second formula of Eq. (3) indicates that the displacement discontinuity in the tangential direction of the cemented surface is proportional to the shear stress of the cemented surface. The third formula of Eq. (3) indicates that the displacement discontinuity in the normal direction is proportional to the normal stress of the cemented surface, and there is no coupling between the shear amount and the normal amount. α and β reflect the mechanical properties of the cemented surface. When $\alpha=0$ and $\beta=0$, it is an ideal cemented surface. When $\alpha\neq 0$ and $\beta=0$, the cemented surface only slides in the tangential direction under the action of an external force, and it does not open in the normal direction. When $\alpha\to\infty$ and $\beta\to0$, it represents free sliding on the cemented surface. When

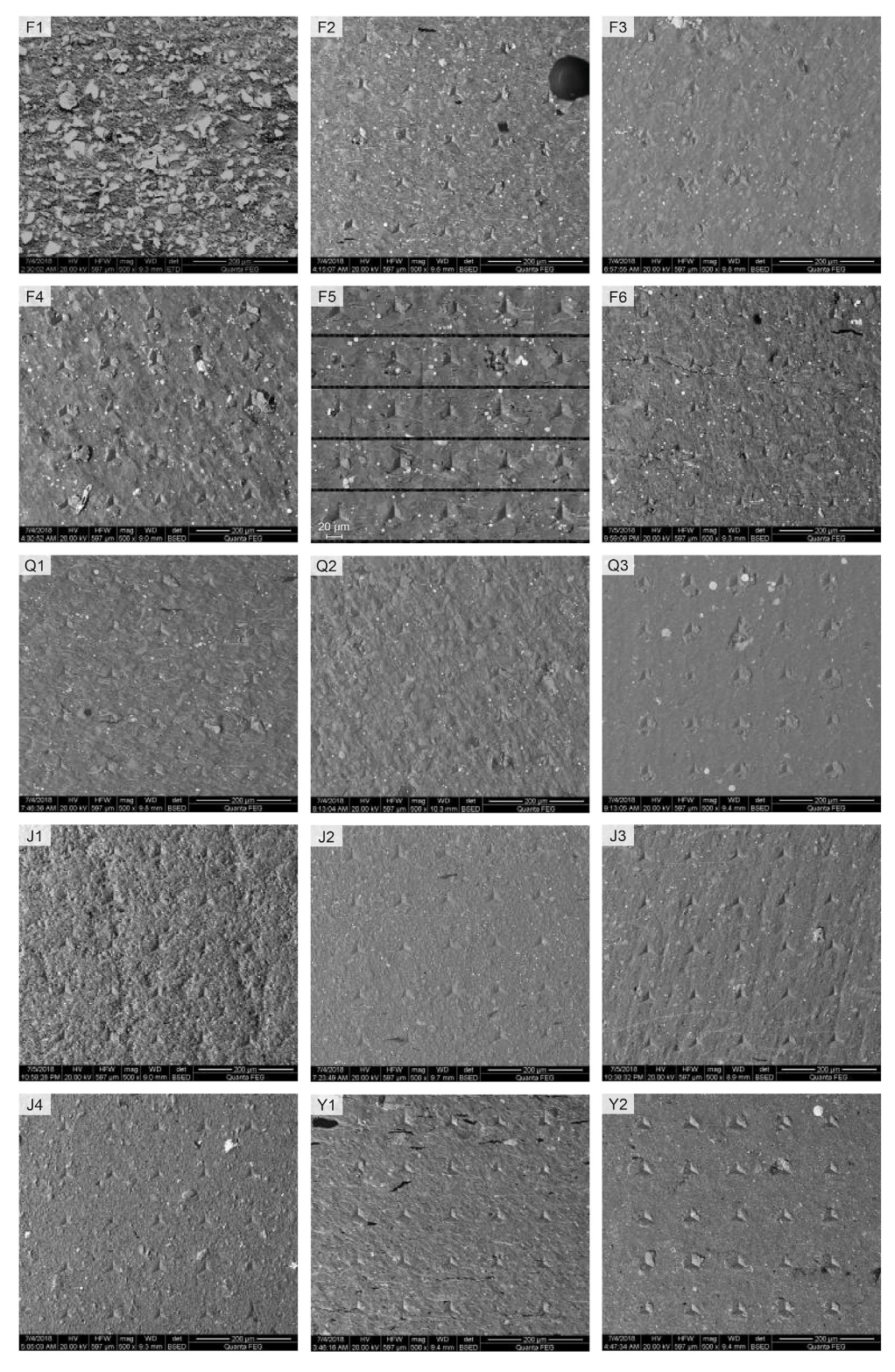


Fig. 9. SEM images of each group of samples after indentation testing.

 $\alpha \to \infty$ and $\beta \to \infty$, it means that the cemented surface is completely separated, and there are no forces between the different phases.

5.2.2. Stress and strain of individual component particles

The solution of the single inclusion problem has special significance for the mesomechanics of composite materials and is the basis for studying the interactions between inclusions and their

influence on the mechanical properties of composite materials. The classic single inclusion solution is the Eshelby solution of elliptic inclusions (Eshelby, 1957). However, because it assumes that the cementation surface is ideally cemented, it is not suitable for situations where the cementation surface has displacement discontinuities. In this work, the spherical inclusion model of the linear-spring-type weak cementation surface was adopted. The hard

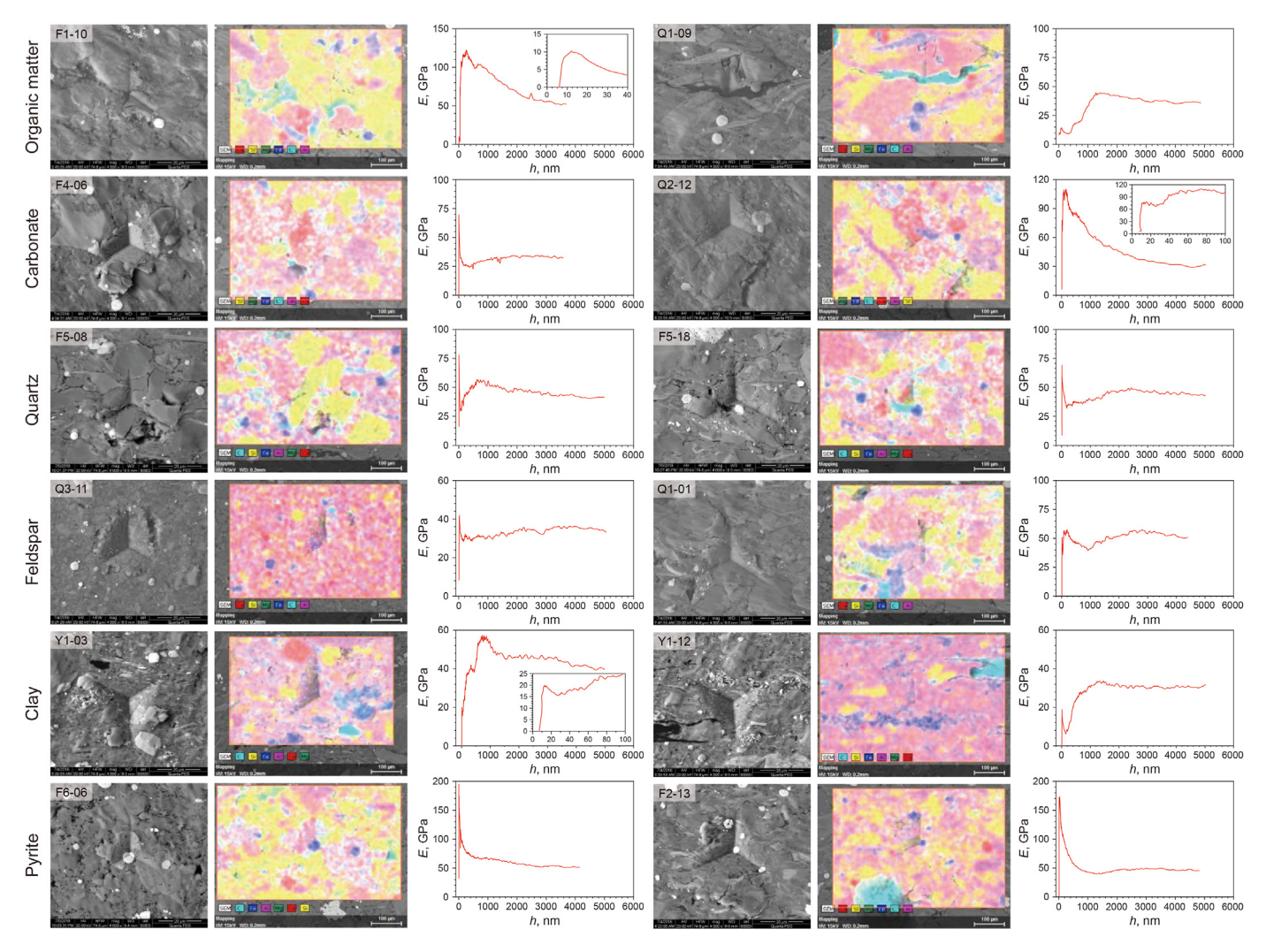


Fig. 10. SEM-EDS images and indentation depth vs. elastic modulus curves of different mineral. The data are from one of the 25 tests conducted on each sample, where F1-10 refers to the curve of the tenth test of sample F1 in Fig. 7.

component mineral particles in the rock were assumed to be spherical, and there was a weak interface between the hard components and the soft components (matrix). Then, under the action of a far-field uniform stress, the average stress and average strain inside the hard component particles are respectively

$$\begin{cases} \sigma_{ij}^{-r} = A_{ijkl} \sigma_{kl}^{0} \\ \varepsilon_{ij}^{-r} = C_{ijkl}^{*-1} \sigma_{kl}^{-r} \end{cases}$$

$$(4)$$

with

$$A_{ijkl} = \frac{A_1}{3} \delta_{ij} \delta_{kl} + \frac{A_2}{2} \left(\delta_{ik} \delta_{jl} + \delta_{il} \delta_{jk} - \frac{2}{3} \delta_{ij} \delta_{kl} \right) \tag{5}$$

The displacement discontinuity of the corresponding cemented surface is

$$[\mu_{\rm i}] = -\frac{\lambda_2(1-2\nu_{\rm m})}{6\mu_{\rm m}(1+\nu_{\rm m})}\sigma_{\rm ll}^0x_{\rm i} - A_1\frac{s_{\rm ij}^0}{2\mu_{\rm m}}x_{\rm j} - \frac{B_1}{a^2}\frac{s_{\rm kl}^0}{2\mu_{\rm m}}x_{\rm i}x_{\rm k}x_{\rm l} \tag{6}$$

where x_i is the coordinate; C_{ijkl}^{*-1} represents the components of the elastic tensor of the hard components; μ_m and ν_m are the shear modulus and Poisson's ratio of the soft components, respectively;

 $\sigma_{\rm kl}^0$ is the far-field uniform stress; $S_{\rm kl}^0$ is the skewed part of $\sigma_{\rm ij}^0$; and a is the radius of a spherical hard component particle. The parameters in Eqs. (5) and (6) (Λ_1 , Λ_2 , λ_1 , Λ_1 , and B_1) are related to the elastic modulus of the hard components, the elastic modulus of the soft components, and the flexibility of the cemented surface. See Appendix A for the solution method.

5.2.3. Multiphase composite media model for rocks with weak cementation surfaces

For the macroscopic scale of rock multiphase composite media, the average stress and average strain are

$$\begin{cases}
\overline{\sigma}_{ij} = f \sigma_{ij}^{-r} + (1 - f) \sigma_{ij}^{-m} \\
\overline{\varepsilon}_{ij} = f \varepsilon_{ij}^{-r} + (1 - f) \varepsilon_{ij}^{-m} + \frac{1}{2V} \int_{S} ([u_i] n_j + [u_j] n_i) ds
\end{cases} (7)$$

where $\overline{\sigma}_{ij}$ and $\overline{\varepsilon}_{ij}$ are the average stress and average strain of the hard components, respectively; σ_{ij}^{-m} and ε_{ij}^{-m} are the mean stress and mean strain of the soft components, respectively; $[u_i]$ is the displacement discontinuity between both sides of the weak cementation surface; V is the total volume of the rock; and f is the volume content of the hard components. These sum to 100% with the volume content of the soft components, as shown in Fig. 15. The

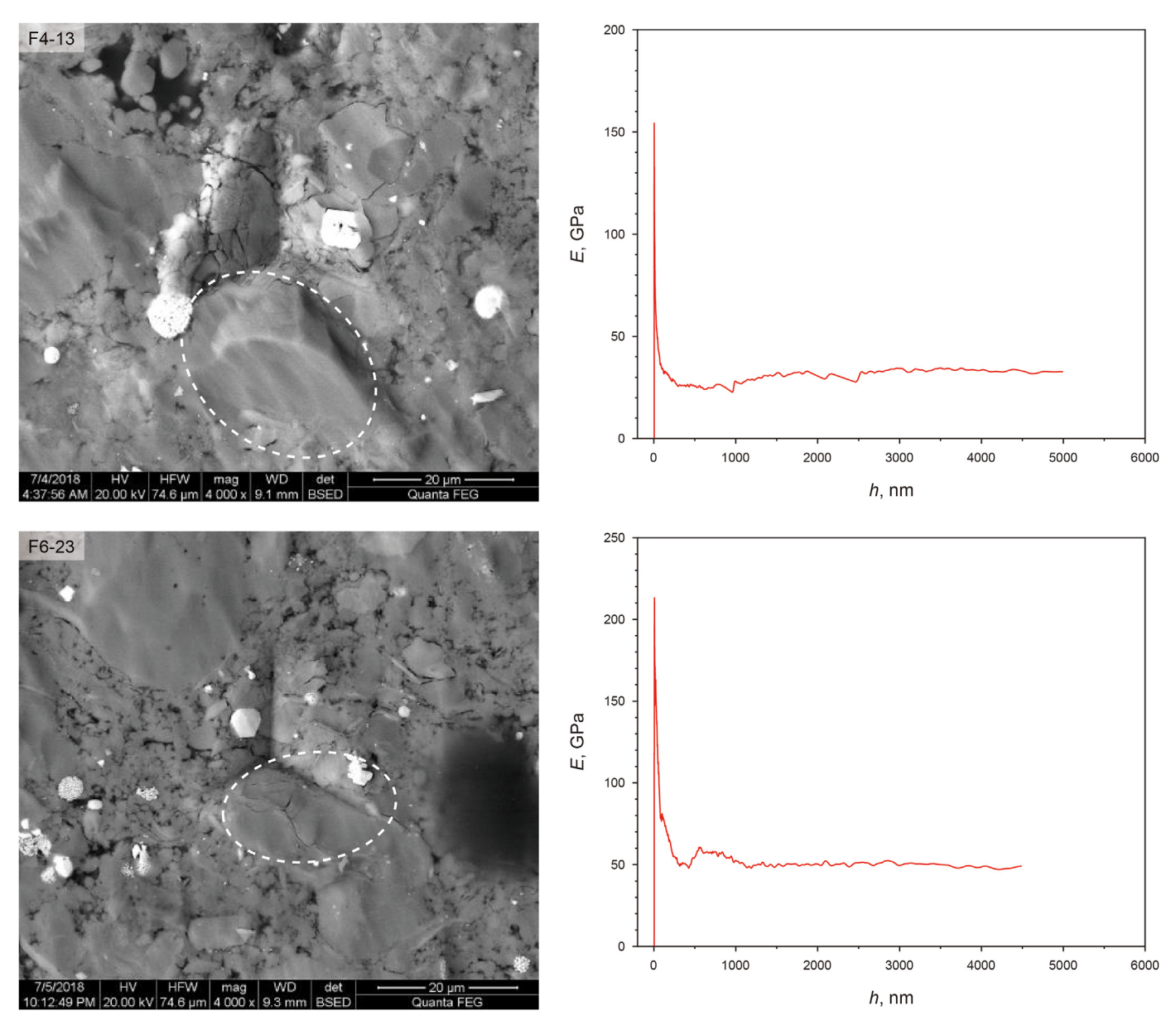


Fig. 11. Abnormal indentation point image and indentation depth vs. elastic modulus curves caused by insufficient surface flatness of the sample.

area integration domain *S* includes all weak cementation surfaces in the rock. The effective modulus of elasticity of the composite medium was obtained by the following formula:

$$\overline{\sigma}_{ii} = \overline{C}_{iikl}\overline{\varepsilon}_{kl} \tag{8}$$

When the far-field provides a uniform stress σ_{ij}^0 , then $\overline{\sigma}_{ij}=\sigma_{ij}^0$. Set $\sigma_{ij}^r=R_{ijkl}\sigma_{ij}^0$ and $[u_i]=\phi_{ikl}\sigma_{kl}^0$. From Eqs. (7) and (8), we can obtain

$$\overline{D}_{ijkl} = D^{m}_{ijkl} - f\left(H_{ijkl} - h_{ijkl}\right) \tag{9}$$

$$\begin{cases} H_{ijkl} = \left(D_{ijpq}^{m} - D_{ijpq}^{r}\right) R_{pqkl} \\ h_{ijkl} = \frac{1}{2V_{r}} \int_{V_{r}} \left(\phi_{ikl,j} + \phi_{jkl,i}\right) dV \end{cases}$$
(10)

where R_{pqkl} is the component of the stress concentration factor tensor at the edges of the hard components; D_{ijkl}^{r} , D_{ijkl}^{m} , and \overline{D}_{ijkl} are the components of the flexibility tensor of the hard components, soft components, and multiphase composite medium, respectively, which satisfy $C_{ijpq}D_{pqkl} = I_{ijkl}$. By solving for R_{pqkl} and ϕ_{ikl} , the effective elastic modulus of the weak cementation rock can be calculated using Eq. (9).

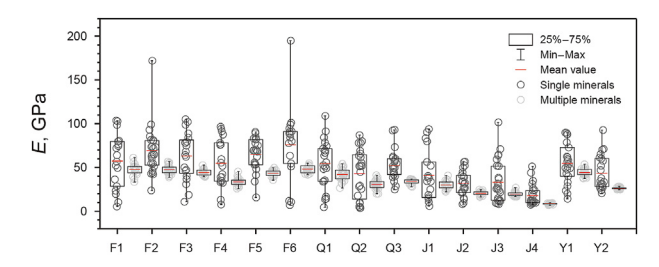


Fig. 12. Statistical results of elastic modulus data for single mineral and multiphase mineral complexes calculated at different depths of indentation.

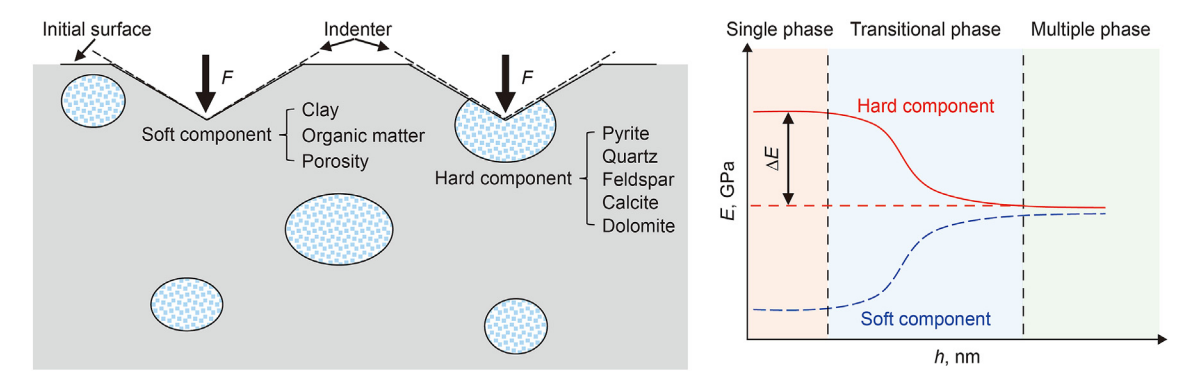


Fig. 13. Schematic diagram of forces at different pressing positions.

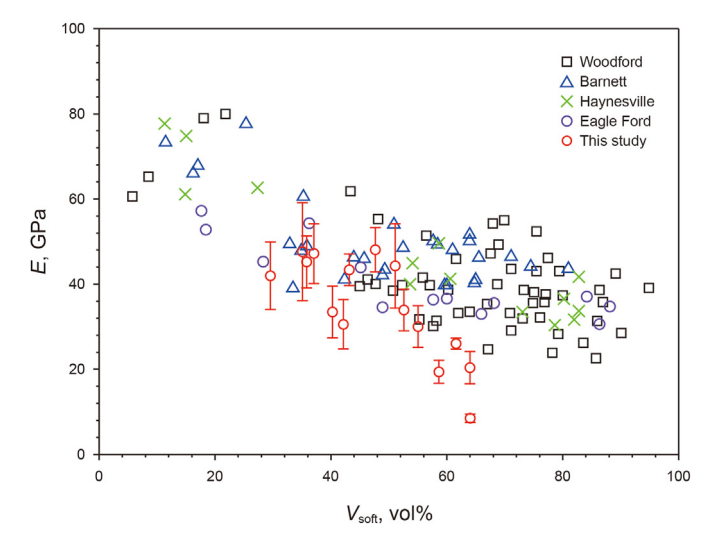


Fig. 14. Correlation analysis between volume content and macroscopic elastic modulus of shale soft components (Shukla et al., 2013).

The Mori-Tanaka method is a relatively concise theoretical method with a clear physical meaning. In this paper, the weak

cemented surface is included as an improvement, which is a possible method to predict the mechanical parameters of rock multiphase composite media. When a hard component is introduced into the multiphase composite medium, the far-field stress and far-field strain of the hard component are the average stress and average strain of the soft components, respectively, i.e., $\sigma_{\rm kl}^0=\sigma_{\rm kl}^{-m}$. Then, according to Eq. (4), the average stress of the hard components is

$$\sigma_{ij}^{-r} = \Lambda_{ijkl}\sigma_{kl}^{-m} \tag{11}$$

The stress concentration factor tensor of the hard components is

$$R_{ijkl} = A_{ijkl} r_{mnkl}^{-1} \tag{12}$$

with

$$r_{ijkl} = (1 - f)I_{ijkl} + f\Lambda_{ijkl}$$

$$\tag{13}$$

The displacement discontinuity between both sides of the interface is

$$[\mu_i] = \phi_{ikl} \sigma^0_{kl} \tag{14}$$

with

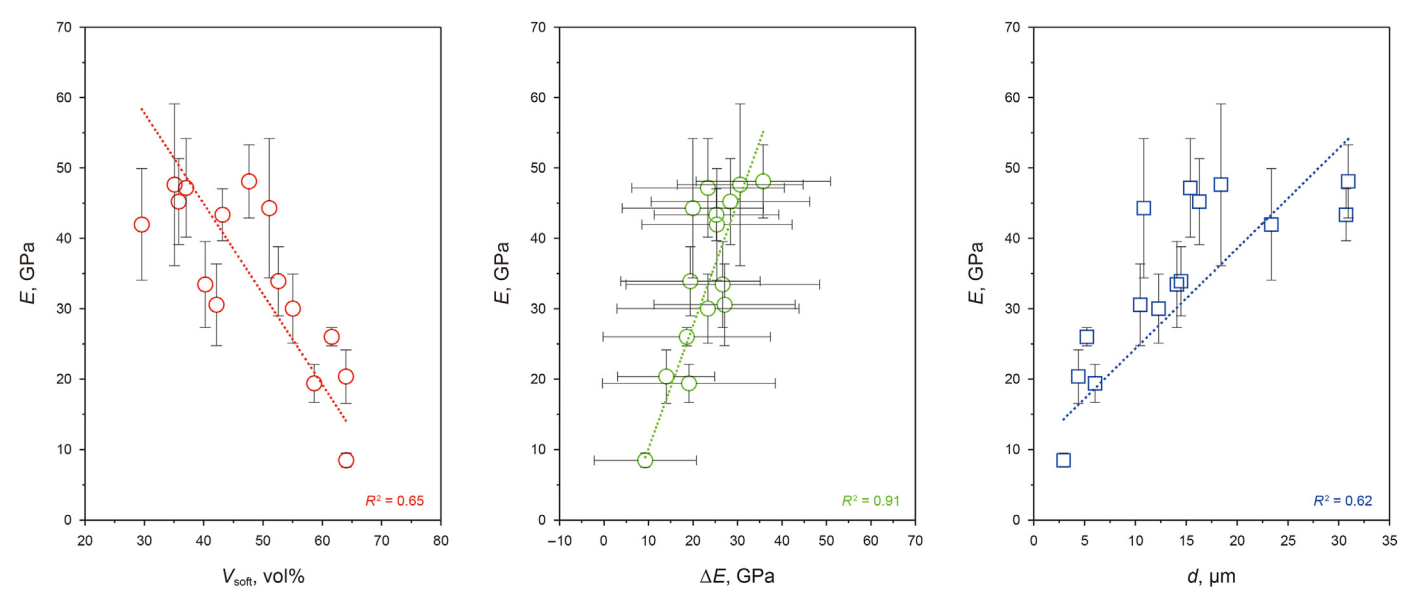


Fig. 15. Correlation analysis of volume content of shale soft components, ΔE , and mineral particle size with macroscopic elastic modulus.

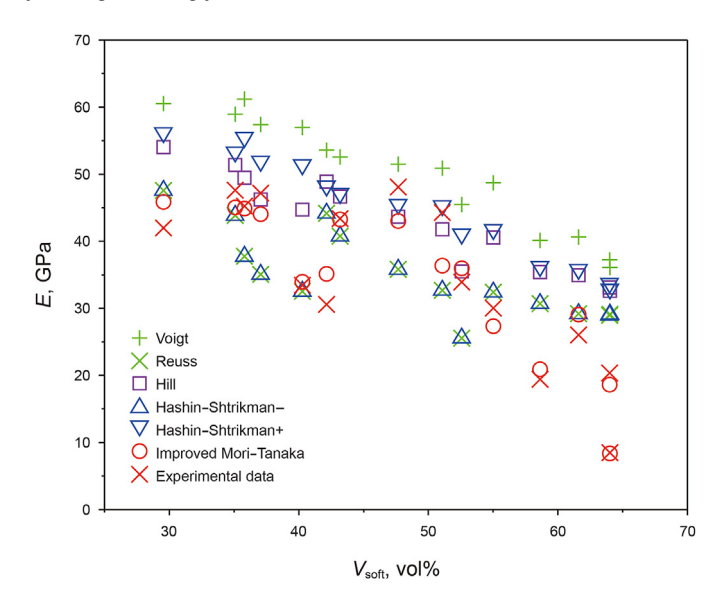


Fig. 16. Error analysis of prediction results and experimental test data of different models.

$$\phi_{ikl} = \frac{1}{2\mu} \left[\frac{1}{3} \left(A_1 + B_1 - \frac{1 - 2\nu_{\rm m}}{1 + \nu_{\rm m}} \lambda_2 \right) \delta_{\rm mn} x_i - A_1 \delta_{im} x_n - \frac{B_1}{a^2} x_i x_m x_n \right] r_{\rm mnkl}^{-1}$$
(15)

Therefore, the bulk modulus of the weak cemented multiphase composite medium can be obtained from Eq. (9), as follows:

$$\frac{K}{K^{\rm m}} = \frac{1 - f + f \Lambda_1}{1 - f - f \lambda_2 + f \Lambda_1 \frac{K^{\rm m}}{K^{\rm r}}} \tag{16}$$

Furthermore, through the conversion formula between the moduli $E=3K(1-2\nu)$, the elastic modulus of the multiphase composite medium of weak cemented rock was obtained. The calculation formulas for parameters \varLambda_1 and \varLambda_2 are as follows:

$$\begin{cases} A_{1} = 1 - \frac{2(1 - 2\nu)}{3(1 - \nu)} (\lambda_{1} - \lambda_{2}) \\ A_{2} = 1 - \frac{7 - 5\nu}{15(1 - \nu)} \left[\left(P_{1} + \frac{2}{5}Q_{1} + \frac{3}{5}N_{1} - A_{1} - \frac{2}{5}B_{1} \right) \right] \end{cases}$$
(17)

Table 2 Standard error analysis table.

Sample No. Standard error, % Voigt Reuss Hill Hashin-Shtrikman-Hashin-Shtrikman+ Improved Mori-Tanaka F1 23.73 7.90 11.93 5.43 F2 21.67 25.70 2.02 25.70 10.12 6.59 F3 35.31 16.54 9.39 16.54 22.70 0.76 F4 33.77 2.79 70.32 2.79 53.69 1.48 F5 21 25 5 98 5 98 8 74 0.24 7 63 F6 7.07 25.57 9.25 25.57 5.32 10.57 Q1 44.15 13.36 28.75 13.36 33.92 9.27 Q2 Q3 J1 75.27 44.43 59.85 44.43 57.75 14.88 24.70 33 99 24.70 4 65 21.05 6.01 62.23 7.91 35.07 7.91 38.98 9.04 J2 J3 J4 Y1 82.98 42.18 62.58 42.18 65.73 8.57 106.78 58.23 82.51 58.23 86.92 7.78 324.96 242.94 283.95 242.94 287.13 1.41 14 98 26.20 5.61 26.20 2.36 17 90 12.21 37.68 56.25 12.21 34.23 11.72

5.3. Prediction results using weak cementation model

In the multiphase composite medium model of weak cemented rock, some key parameters needed to be obtained before the calculation of the macroscopic mechanical parameters. As shown in Eq. (16), it was necessary to know the volume content of the hard components in the rock f, which were obtained from the data shown in Table 1. It should be noted that when performing this calculation, the volume content needed to be converted into a value between 0 and 1 to make it dimensionless. The mechanical parameters (K^r and K^m) of the hard and soft components in Eq. (16) were obtained from the test results shown in Fig. 10 and the modulus conversion formula. The parameters Λ_1 and λ_2 needed to be calculated by the formula shown in Appendix A. The formula includes two-variable linear and six-variable linear equations, and the solution is shown in Eqs. (A1)—(A4).

In particular, it should be noted that the weak interface of the rock was mainly reflected in the parameters α_0 and β_0 , and the formulas are as follows:

$$\begin{cases} \alpha_0 = \frac{\alpha \mu_{\rm m}}{a} \\ \beta_0 = \frac{\beta \mu_{\rm m}}{a} \end{cases}$$
 (18)

where α_0 and β_0 are respectively the shear flexibility coefficient and the normal flexibility coefficient of the cemented surface between the hard and soft components; and $\mu_{\rm m}$ was calculated by the modulus conversion formula $\mu_{\rm m} = \frac{E_{\rm m}}{2+2\nu_{\rm m}}$.

Microscopically, the shear flexibility and normal flexibility of the cemented surface was considered to be consistent, and thus, $\alpha=\beta$. As mentioned in Section 4 above, the modulus of the cementation surface was ΔE and its reciprocal was the flexibility. Then, α and β were set to $\frac{1}{\Delta E}$. The particle size a of the hard components was obtained from Fig. 1. By substituting the data of each sample group in the nanoindentation experiment, the shear flexibility coefficient of each group was obtained. In the formula, experimental values of $E_{\rm r}$ and $E_{\rm m}$ were used, and the average value of the single-mineral elastic moduli of quartz, feldspar, calcite, and dolomite was set as $E_{\rm r}$. Also, the single-component elastic modulus average was set as $E_{\rm m}$ for clay and organic matter. Since the elastic modulus of pyrite was too high and its content was small, it was not included in the average value of the elastic modulus of the hard components. The pores did not have an elastic modulus and were not included in the

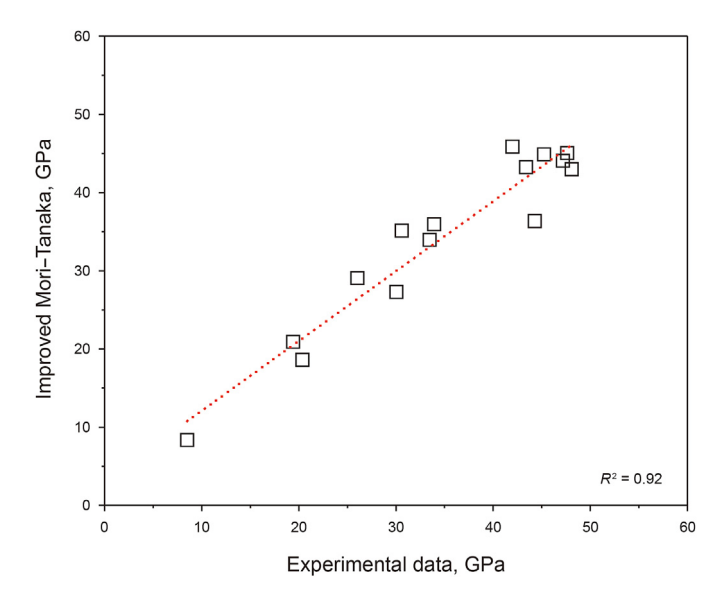


Fig. 17. Improved Mori-Tanaka model and fitting analysis of experimental test data.

soft component elastic modulus calculation. ν_r and ν_m had the values of 0.25 and 0.3, respectively.

Based on Eq. (14) in the previous text and the formulas shown in Appendix A, the volume content of the components in shale, the single-phase mechanical parameters, the cementation strength, and the mineral particle size, the shale macroscopic elastic modulus was calculated. As shown in Fig. 15, the prediction results were in good agreement with the experimental data. The error results in Table 2 also show that the error was between 0.24% and 17.90%. While the errors of most calculation results are improved, the errors of F6, Q2, Y1, and Y2 data are larger. We carefully analyze the data and find that the calculated elastic modulus using the prediction model described in this paper is greater than the measured value. The reason is that the test results of cementation strength in this paper are high, and we estimate that the number of test indentations is too small. In the future, the accuracy of the calculation method in this paper can be improved by increasing the sample size. Compared with the prediction errors of 2.36%-324.96% for the model without considering the weak cementation surface, the accuracy was improved. The experimental data were fitted with the proposed model, as shown in Fig. 17, and the fitting degree reached 0.92. The physical meaning of the weak cementation surface model is clear, the parameters are easy to obtain, and the prediction accuracy is high. Thus, it can be popularized and applied in engineering.

6. Conclusions

In this paper, the elastic modulus of shale in the indentation depth range of 0–5000 nm was obtained through nanoindentation experiments on 15 groups of shale samples, and a prediction model for the macroscopic mechanical parameters was constructed. The following conclusions were obtained.

(1) Different depths have different physical properties. Shallower depths have the mechanical properties of a single mineral, while deeper depths have the mechanical properties of a multi-mineral composite. The difference of elastic modulus between single and multi-mineral hard components can be used to characterize the cementation strength between mineral particles.

- (2) The main controlling factors of the shale macroscopic elastic modulus are the mineral components of shale (such as the volume contents of the soft components, e.g., clay, organic matter, and pores), the cementation strength between particles, and the mineral particle size.
- (3) Compared with the calculation data of the existing rock mechanics parameter model, it is found that the error is as high as 324.96%. The calculated result is larger than the experimental value, so the problem of weak cementation between mineral particles should be considered.
- (4) Based on the existing weak cementation model, the three parameters of soft component volume content, interparticle cementation strength, and mineral particle size tested by nanoindentation experiment are substituted to achieve the high-precision prediction of shale macroscopic mechanical parameters, and the error is reduced to less than 17.90%. The test method and calculation model can be widely used in engineering.

CRediT authorship contribution statement

Jian-Bo Wang: Writing — review & editing, Writing — original draft, Methodology, Data curation, Conceptualization. **Yang-Yang Zhang:** Data curation, Formal analysis, Methodology, Software. **Jian-Tong Liu:** Writing — review & editing, Data curation, Conceptualization. **Xiao-Di Li:** Writing — review & editing, Methodology, Formal analysis. **Bo Zhou:** Data curation. **Yuan-Kai Zhang:** Project administration. **Bao-Xing Liang:** Conceptualization.

Data availability statement

Figures were prepared using Origin Software Tools. All data related to these figures are available at https://datadryad.org/stash/share/

BNIBC152T9uYhjPx16xLi8QtpaXp51RaxwQZqofFfQ4.

Declaration of compting interest

The authors declare no conflicts of interest relevant to this study.

Acknowledgments

This work was supported by the Key R&D Program Project of Xinjiang Province (2024B01013) and the National Key Research and Development Program of China (2022YFE0129800).

Appendix A

To obtain the parameters required in the model proposed in this paper, the model of weakly cemented surfaces in the mechanics of materials was used. The formula includes two-dimensional linear and six-dimensional linear equations, shown as follows:

(A3)

$$\begin{cases} g_{11} = \frac{2(1-2\nu^m)}{1-\nu^m} + \frac{1-2\nu^m}{(l+\nu^m)(\rho_1 - 3\rho_2)} & g_{12} = \frac{2(1-2\nu^m)}{3(1-\nu^m)} & g_{22} = \frac{2(1-2\nu^m)}{3(1-\nu^m)} & g_{22}$$

$$\begin{cases} \rho_1 = \frac{\mu^{m}}{\mu^{r}} - 1 \\ \rho_2 = \frac{\mu^{m} v^{r}}{\mu^{r} (1 + v^{r})} - \frac{v^{m}}{1 + v^{m}} \end{cases}$$
(A4)

References

Abedi, S., Slim, M., Ulm, F., 2016. Nanomechanics of organic-rich shales: the role of thermal maturity and organic matter content on texture. Acta Geotechnica 11, 775–787. https://doi.org/10.1007/s11440-016-0476-2.

Abousleiman, Y., Tran, M., Hoang, S., Ortega, J.A., 2010. Geomechanics field characterization of Woodford Shale and Barnett Shale with advanced logging tools and nano-indentation on drill cuttings. Lead. Edge 29 (6), 730–736. https://doi.org/10.1190/1.3447787.

Auvray, C., Lafrance, N., Bartier, D., 2017. Elastic modulus of claystone evaluated by nano-/micro-indentation tests and meso-compression tests. J. Rock Mech. Geotech. Eng. 9 (1), 84–91. https://doi.org/10.1016/j.jrmge.2016.02.002.

Balko, J., Csanádi, T., Sedlák, R., Vojtko, M., Kovalkíková, A., Koval, K., Wyzga, P., Naughton, A., 2017. Nanoindentation and tribology of VC, NbC and ZrC refractory carbides. J. Eur. Ceram. Soc. 37 (14), 4371–4377. https://doi.org/10.1016/j.jeur.ceramsoc.2017.04.064.

Bei, H., George, E.P., Hay, J., Pharr, G., 2005. Influence of indenter tip geometry on elastic deformation during nanoindentation. Phys. Rev. Lett. 95 (4), 045501. https://doi.org/10.1103/PhysRevLett.95.045501.

Benveniste, Y., 1985. The effective mechanical behaviour of composite materials with imperfect contact between the constituents. Mech. Mater. 4 (2), 197–208. https://doi.org/10.1016/0167-6636(85)90016-x.

Bobko, C., Ulm, F., 2008. The nano-mechanical morphology of shale. Mech. Mater. 40 (4–5), 318–337. https://doi.org/10.1016/j.mechmat.2007.09.006.

Britt, L.K., Schoeffler, J., 2009. The geomechanics of a shale play: what makes a shale prospective!. In: SPE Eastern Regional Meeting. https://doi.org/10.2118/125525-MS

Carreño, P., Pérez, T., Marfisi, N., Gomez, J.J., Pérez, C., 2018. Integrated methodology for laboratory evaluation of shale plays cuttings. In: SPE Argentina Exploration and Production of Unconventional Resources Symposium. https://doi.org/ 10.2118/191812-MS.

Cipolla, C.L., Warpinski, N.R., Mayerhofer, M.J., 2008. Hydraulic fracture complexity: diagnosis, remediation, and exploitation. In: SPE Asia Pacific Oil and Gas Conference and Exhibition. https://doi.org/10.2118/115771-MS.

Curtis, J., 2002. Fractured shale-gas systems. AAPG Bull. 86 (11), 1921–1938. https://doi.org/10.1306/61eeddbe-173e-11d7-8645000102c1865d.

Deirieh, A., Ortega, J., Ulm, F., 2012. Nanochemomechanical assessment of shale: a coupled WDS-indentation analysis. Acta Geotechnica 7, 271–295. https:// doi.org/10.1007/s11440-012-0185-4.

Do, H., Dai, V.T., Tian, J.S., Yen, T.C., Chang, L., 2014. Structural and nanoindentation studies of epitaxial titanium oxynitride (001) films grown on MgO (001) substrate. Surf. Coating. Technol. 251, 1–6. https://doi.org/10.1016/j.surfcoat.2014.03.058.

Eshelby, J.D., 1957. The determination of the elastic field of an ellipsoidal inclusion, and related problems. Surf. Coating. Technol. 241 (1226), 376–396.
Faghihi, D., Voyiadjis, G., 2012. Determination of nanoindentation size effects and

Faghihi, D., Voyiadjis, G., 2012. Determination of nanoindentation size effects and variable material intrinsic length scale for body-centered cubic metals. Mech. Mater. 44, 189–211. https://doi.org/10.1016/j.mechmat.2011.07.002.
 Fan, M., Jin, Y., Chen, M., Geng, Z., 2019. Mechanical characterization of shale

Fan, M., Jin, Y., Chen, M., Geng, Z., 2019. Mechanical characterization of shale through instrumented indentation test. J. Petrol. Sci. Eng. 174, 607–616. https:// doi.org/10.1016/j.petrol.2018.11.083.

Fisher, M., Heinze, J., Harris, C., Davidson, B., Wright, C., Dunn, K., 2004. Optimizing horizontal completion techniques in the Barnett Shale using microseismic fracture mapping. In: SPE Annual Technical Conference and Exhibition. https:// doi.org/10.2118/90051-MS.

Gao, Z., Hu, Q.J.A.B., 2018. Pore structure and spontaneous imbibition characteristics of marine and continental shales in China. AAPG (Am. Assoc. Pet. Geol.) Bull. 102 (10), 1941–1961. https://doi.org/10.1306/03291817297.

(10), 1941–1961. https://doi.org/10.1306/03291817297.

Giraud, A., Huynh, Q.V., Hoxha, D., Kondo, D., 2007. Application of results on Eshelby tensor to the determination of effective poroelastic properties of anisotropic rocks-like composites. International Journal of Solids and Structure 44 (11–12), 3756–3772. https://doi.org/10.1016/j.ijsolstr.2006.10.019.

Goktan, R.M., Gunes, N., 2005. A new methodology for the analysis of the relationship between rock brittleness index and drag pick cutting efficiency. Journal of the Southern African Institute of Mining and Metallurgy 105 (10), 727–733. Gommers, B., Verpoest, I., Van Houtte, P.J.A.M., 1998. The Mori–Tanaka method

Gommers, B., Verpoest, I., Van Houtte, P.J.A.M., 1998. The Mori—Tanaka method applied to textile composite materials. Acta Mater. 46 (6), 2223—2235. https:// doi.org/10.1016/s1359-6454(97)00296-6.

Grieser, B., Bray, J., 2007. Identification of production potential in unconventional reservoirs. In: Production and Operations Symposium. https://doi.org/10.2118/ 110632-MS

Guo, J., Zhao, Z., He, S., Liang, H., Liu, Y., 2015. A new method for shale brittleness

evaluation. Environ. Earth Sci. 73, 5855—5865. https://doi.org/10.1007/s12665-015-4268-z.

- Hashin, Z., 1991. The spherical inclusion with imperfect interface. J. Appl. Mech. 444–449. https://doi.org/10.1115/1.2897205.
- Herrmann, J., Rybacki, E., Sone, H., Dresen, G., 2018. Deformation experiments on Bowland and Posidonia Shale—part I: strength and Young's modulus at ambient and in situ *p_c*—*T* conditions. Rock Mech. Rock Eng. 51, 3645—3666. https://doi.org/10.1007/s00603-018-1572-4.
- Hu, Q., Chen, X., Guo, Y., 2013. A rock physics model of kerogen inclusions in shale. In: SEG International Exposition and Annual Meeting. https://doi.org/10.1190/segam2013-1023.1.
- Jenkins, C., Boyer, C., 2008. Coalbed-and shale-gas reservoirs. J. Petrol. Technol. 60 (2), 92-99. https://doi.org/10.2118/103514-JPT.
- Jiang, X., Han, X., Cui, Z., 2007. New technology for the comprehensive utilization of Chinese oil shale resources. Energy 32 (5), 772–777. https://doi.org/10.1016/ i.energy.2006.05.001.
- Kabir, P., Ulm, F., Akono, A., 2017. Rate-independent fracture toughness of gray and black kerogen-rich shales. Acta Geotechnica 12, 1207–1227. https://doi.org/ 10.1007/s11440-017-0562-0.
- Kenechukwu, C., Prasad, M., Batzle, M.L., 2010. The maturity of organic-rich shales using microimpedance analysis. In: SPE Annual Technical Conference and Exhibition. https://doi.org/10.2118/135569-MS.
- Khatibi, S., Ostadhassan, M., Tuschel, D., Gentzis, T., Bubach, B., Carvajal-Ortiz, H., 2018. Raman spectroscopy to study thermal maturity and elastic modulus of kerogen. Journal of Coal Geology 185, 103–118. https://doi.org/10.1016/ i.coal.2017.11.008.
- King, G.E., 2010. Thirty years of gas shale fracturing: what have we learned?. In: SPE Annual Technical Conference and Exhibition. https://doi.org/10.2118/133456-MS.
- Kohli, A.H., Zoback, M.D., 2013. Frictional properties of shale reservoir rocks. J. Geophys. Res. Solid Earth 118 (9), 5109-5125. https://doi.org/10.1002/jgrb.50346.
- Kumar, V., 2012. Geomechanical Characterization of Shale Using Nano-Indentation. Doctoral Dissertation. University of Oklahoma, Norman, OK, USA.
- Kumar, V., Curtis, M.E., Gupta, N., Sondergeld, C.H., Rai, C.S., 2012a. Estimation of elastic properties of organic matter and Woodford shale through nanoindentation measurements. In: SPE Canada Unconventional Resources Conference. https://doi.org/10.2118/162778-MS.
- Kumar, V., Sondergeld, C., Rai, C.S., 2015. Effect of mineralogy and organic matter on mechanical properties of shale. Interpretation 3 (3), SV9—SV15. https://doi.org/ 10.1190/INT-2014-0238.1.
- Kumar, V., Sondergeld, C.H., Rai, C.S., 2012b. Nano to macro mechanical characterization of shale. In: SPE Annual Technical Conference and Exhibition. https:// doi.org/10.2118/159804-MS.
- Landman, U., Luedtke, W., Burnham, N.A., Colton, R., 1990. Atomistic mechanisms and dynamics of adhesion, nanoindentation, and fracture. Science 248 (4954), 454–461. https://doi.org/10.1126/science.248.4954.454.
- Li, C., Ostadhassan, M., Kong, L., Bubach, B., 2019. Multi-scale assessment of mechanical properties of organic-rich shales: a coupled nanoindentation, deconvolution analysis, and homogenization method. J. Petrol. Sci. Eng. 174, 80—91. https://doi.org/10.1016/j.petrol.2018.10.106.
- Li, W., Sakhaee-Pour, A., 2016. Macroscale Young's moduli of shale based on nanoindentations. Petrophysics 57 (6), 597–603.
- Li, X., Gao, H., Murphy, C., Caswell, K., 2003. Nanoindentation of silver nanowires. Nano Lett. 3 (11), 1495–1498. https://doi.org/10.1021/nl034525b.
- Li, Y., Chen, J., Yang, J., Liu, J., Tong, W., 2022. Determination of shale macroscale modulus based on microscale measurement: a case study concerning multiscale mechanical characteristics. Pet. Sci. 19 (3), 1262–1275. https://doi.org/ 10.1016/j.petsci.2021.10.004.
- Liu, K., Jin, Z., Zakharova, N., Zeng, L., Haghshenas, M., Adeyilola, A., Saurabh, S., 2023. Comparison of shale fracture toughness obtained from scratch test and nanoindentation test. Int. J. Rock Mech. Min. Sci. 162, 105282. https://doi.org/ 10.1016/j.ijrmms.2022.105282.
- Liu, K., Ostadhassan, M., Bubach, B., 2016. Applications of nano-indentation methods to estimate nanoscale mechanical properties of shale reservoir rocks. Gas Science and Engineering 35, 1310–1319. https://doi.org/10.1016/ j.jngse.2016.09.068.
- Liu, N., Fu, L., 2020. Elastic characteristics of digital cores from Longmaxi shale using lattice spring models. Commun. Comput. Phys. 28 (1), 518-538. https://doi.org/ 10.4208/cicp.OA-2018-0085.
- Liu, Y., 2015. Fracture Toughness Assessment of Shales by Nanoindentation. https://doi.org/10.7275/jzym-1g18.
- Liu, Y., Sokolov, I., Dokukin, M., Xiong, Y., 2020. Can AFM be used to measure absolute values of Young's modulus of nanocomposite materials down to the nanoscale? Nanoscale 12 (23), 12432–12443. https://doi.org/10.1039/d0nr02314k.
- Luo, S., Kim, D., Wu, Y., Li, Y., Wang, D., Song, J., DeGroot, D.J., Zhang, G., 2021. Big data nanoindentation and analytics reveal the multi-staged, progressively-homogenized, depth-dependent upscaling of rocks' properties. Rock Mech. Rock Eng. 54, 1501–1532. https://doi.org/10.1007/s00603-020-02337-3.
- Luo, S., Lu, Y., Wu, Y., Song, J., DeGroot, D.J., Jin, Y., Zhang, G., 2020. Cross-scale characterization of the elasticity of shales: statistical nanoindentation and data analytics. J. Mech. Phys. Solid. 140, 103945. https://doi.org/10.1016/ j.jmps.2020.103945.
- Ma, X., Wang, H., Zhou, S., Shi, Z., Zhang, L., 2021a. Deep shale gas in China:

- geological characteristics and development strategies. Energy Rep. 7, 1903–1914. https://doi.org/10.1016/j.egyr.2021.03.043.
- Ma, X., Xie, J., 2018. The progress and prospects of shale gas exploration and development in southern Sichuan Basin, SW China. Petrol. Explor. Dev. 45 (1), 172–182. https://doi.org/10.1016/S1876-3804(18)30018-1.
- Ma, Z., Gamage, R., Zhang, C., 2021b. Mechanical properties of α-quartz using nanoindentation tests and molecular dynamics simulations. Int. J. Rock Mech. Min. Sci. 147, 104878. https://doi.org/10.1016/j.ijrmms.2021.104878.
- Martineau, D.F., 2007. History of the newark east field and the Barnett shale as a gas reservoir. AAPG (Am. Assoc. Pet. Geol.) Bull. 91 (4), 399–403. https://doi.org/10.1306/intro910407.
- Matthews, H.L., Schein, G., Malone, M., 2007. Stimulation of gas shales: they're all the same—right?. In: SPE Hydraulic Fracturing Technology Conference and Exhibition. https://doi.org/10.2118/106070-MS.
- Mavko, G., Mukerji, T., Dvorkin, J., 2009. The Rock Physics Handbook. Cambridge University Press.
- Mighani, S., Bernabé, Y., Boulenouar, A., Mok, U., Evans, B., 2019. Creep deformation in Vaca Muerta shale from nanoindentation to triaxial experiments. J. Geophys. Res. Solid Earth 124 (8), 7842—7868. https://doi.org/10.1029/2019jb017524.
- Minor, A.M., Syed Asif, S., Shan, Z., Stach, E.A., Cyrankowski, E., Wyrobek, T.J., 2006.

 A new view of the onset of plasticity during the nanoindentation of aluminium.

 Nat. Mater. 5 (9), 697–702. https://doi.org/10.1038/nmat1714.

 Mullen, M., Roundtree, R., Barree, B., 2007. A composite determination of me-
- Mullen, M., Roundtree, R., Barree, B., 2007. A composite determination of mechanical rock properties for stimulation design (what to do when you don't have a sonic log). In: SPE Rocky Mountain Petroleum Technology Conference. https://doi.org/10.2118/108139-MS.
- Nejad, A.M., Shelley, R.F., Lehman, L.V., Shah, K., Gusain, D., Conway, M.T., 2013. Development of the brittle shale fracture network model. In: SPE Hydraulic Fracturing Technology Conference and Exhibition. https://doi.org/10.2118/ 163829-MS.
- Nezhad, M.M., Zhu, H., Woody Ju, J., Chen, Q., 2016. A simplified multiscale damage model for the transversely isotropic shale rocks under tensile loading. Int. J. Damage Mech. 25 (5), 705–726. https://doi.org/10.1177/1056789516639531.
- Nhabanga, O.J., Ringrose, P.S., Holt, R.M., 2021. Use of rock-physics analysis of well logs to determine compaction history of Cretaceous shales in the Rovuma basin, Offshore Mozambique. Geophys. Prospect. 69 (6), 1282–1294. https://doi.org/10.1111/1365-2478.13104.
- Oliver, W.C., Pharr, G.M., 1992. An improved technique for determining hardness and elastic modulus using load and displacement sensing indentation experiments. J. Mater. Res. 7 (6), 1564–1583. https://doi.org/10.1557/jmr.1992.1564.
- Olson, J.E., 2008. Multi-fracture propagation modeling: applications to hydraulic fracturing in shales and tight gas sands. In: ARMA US Rock Mechanics/Geomechanics Symposium. ARMA-08-327.
- Ortega, J.A., Ulm, F.J., Abousleiman, Y.J., 2007. The effect of the nanogranular nature of shale on their poroelastic behavior. Acta Geotechnica 2, 155–182. https://doi.org/10.1007/s11440-007-0038-8.
- Ortega, J.A., Ulm, F.J., Abousleiman, Y.J.G., 2009. The nanogranular acoustic signature of shale. Geophysics 74 (3), D65–D84. https://doi.org/10.1190/1.3097887.
- Pătru, M., Isac, L., Cunha, L., Martins, P., Lanceros-Mendez, S., Oncioiu, G., Cristea, D., Munteanu, D.J., 2015. Structural, mechanical and piezoelectric properties of polycrystalline AlN films sputtered on titanium bottom electrodes. Appl. Surf. Sci. 354, 267–278. https://doi.org/10.1016/j.apsusc.2015.07.022.
- Qian, K.R., Liu, T., Liu, J.Z., Liu, X.W., He, Z.L., Jiang, D.J., 2020. Construction of a novel brittleness index equation and analysis of anisotropic brittleness characteristics for unconventional shale formations. Pet. Sci. 17 (1), 70–85. https://doi.org/ 10.1007/s12182-019-00372-6.
- Rickman, R., Mullen, M., Petre, E., Grieser, B., Kundert, D., 2008. A practical use of shale petrophysics for stimulation design optimization: all shale plays are not clones of the Barnett shale. In: SPE Annual Technical Conference and Exhibition. https://doi.org/10.2118/115258-MS.
- Rybacki, E., Meier, T., Dresen, G., 2016. What controls the mechanical properties of shale rocks? Part II: brittleness. J. Petrol. Sci. Eng. 144, 39–58. https://doi.org/ 10.1016/j.petrol.2016.02.022.
- Sato, Y., Shinzato, S., Ohmura, T., Hatano, T., Ogata, S., 2020. Unique universal scaling in nanoindentation pop-ins. Nat. Commun. 11 (1), 4177. https://doi.org/10.1038/s41467-020-17918-7.
- Sheng, M., Cheng, S.Z., Lu, Z.H., Zhang, Y., Tian, S.C., Li, G.S., 2022. Influence of formation in-situ stress on mechanical heterogeneity of shale through grid nanoindentation. Pet. Sci. 19 (1), 211–219. https://doi.org/10.1016/j.petsci.2021.10.006.
- Shukla, P., Kumar, V., Curtis, M., Sondergeld, C.H., Rai, C.S., 2013. Nanoindentation studies on shales. In: ARMA US Rock Mechanics/Geomechanics Symposium. ARMA-2013-2578.
- Shukla, P., Taneja, S., Sondergeld, C., Rai, C., 2015. Nanoindentation measurements on rocks. In: Fracture, Fatigue, Failure, and Damage Evolution. Volume 5: Proceedings of the 2014 Annual Conference on Experimental and Applied Mechanics. Springer International Publishing, pp. 99–105. https://doi.org/10.1007/ 978-3-319-06977-7-13.
- Sone, H., Zoback, M.D., 2013a. Mechanical properties of shale-gas reservoir rock-s—Part 1: static and dynamic elastic properties and anisotropy. Geophysics 78 (5), D381–D392. https://doi.org/10.1190/geo2013-0050.1.
- Sone, H., Zoback, M.D., 2013b. Mechanical properties of shale-gas reservoir rock-s—Part 2: ductile creep, brittle strength, and their relation to the elastic modulus. Geophysics 78 (5), D393–D402. https://doi.org/10.1190/geo2013-0051.1.

- Sun, C., Li, G., Gomah, M.E., Xu, J., Sun, Y., 2020. Creep characteristics of coal and rock investigated by nanoindentation. Int. J. Min. Sci. Technol. 30 (6), 769–776. https://doi.org/10.1016/j.ijmst.2020.08.001.
- Tang, X., Jiang, S., Jiang, Z., Li, Z., He, Z., Long, S., Zhu, D., 2019. Heterogeneity of paleozoic wufeng-longmaxi Formation shale and its effects on the shale gas accumulation in the upper yangtze region, China. Fuel 239, 387–402. https:// doi.org/10.1016/j.fuel.2018.11.022.
- Tembe, S., Lockner, D.A., Wong, T.F., 2010. Effect of clay content and mineralogy on frictional sliding behavior of simulated gouges: binary and ternary mixtures of quartz, illite, and montmorillonite. J. Geophys. Res. Solid Earth 115 (B3). https:// doi.org/10.1029/2009jb006383.
- Ulm, F.J., Abousleiman, Y.J.A.G., 2006. The nanogranular nature of shale. Acta Geotechnica 1, 77–88. https://doi.org/10.1007/s11440-006-0009-5.
- Ulm, F.J., Vandamme, M., Bobko, C., Alberto Ortega, J., Tai, K., Ortiz, C.J., 2007. Statistical indentation techniques for hydrated nanocomposites: concrete, bone, and shale. J. Am. Ceram. Soc. 90 (9), 2677–2692. https://doi.org/10.1111/j.1551-2916.2007.02012.x.
- Vasin, R.N., Wenk, H.R., Kanitpanyacharoen, W., Matthies, S., Wirth, R.J., 2013. Elastic anisotropy modeling of Kimmeridge shale. J. Geophys. Res. Solid Earth 118 (8), 3931–3956. https://doi.org/10.1002/jgrb.50259.
- Veytskin, Y.B., Tammina, V.K., Bobko, C.P., Hartley, P.G., Clennell, M.B., Dewhurst, D.N., Dagastine, R., 2017. Micromechanical characterization of shales through nanoindentation and energy dispersive X-ray spectrometry. Geomechanics for Energy and the Environment 9, 21–35. https://doi.org/10.1016/i.gete.2016.10.004.
- Wang, G., Ju, Y., Huang, C., Long, S., Peng, Y., 2017. Longmaxi-Wufeng Shale lith-ofacies identification and 3-D modeling in the northern Fuling gas field, Sichuan Basin. Gas Science and Engineering 47, 59–72. https://doi.org/10.1016/i.ingse.2017.10.003.
- Wang, J., Ge, H., Wang, X., Shen, Y., Liu, T., Zhang, Y., Meng, F., 2019. Effect of clay and organic matter content on the shear slip properties of shale. J. Geophys. Res. Solid Earth 124 (9), 9505–9525. https://doi.org/10.1029/2018jb016830.
- Wang, J., Liu, Y., Yang, C., Jiang, W., Li, Y., Xiong, Y., 2022a. Evolution of mechanical properties of kerogen with thermal maturity. Mar. Petrol. Geol. 145, 105906. https://doi.org/10.1016/j.marpetgeo.2022.105906.
- Wang, T., Wang, Q., Zhang, P., Cheng, S., Anyimah, P.O., Tan, Y., Tian, S., 2022b. Application of atom force microscope and nanoindentation to characterize nanoscale mechanical properties of shale before and after supercritical CO₂ immersion. J. Petrol. Sci. Eng. 212, 110348. https://doi.org/10.1016/ j.petrol.2022.110348.
- Wang, Z., Zhang, Q., Liu, J., Fu, L., 2021. Effective moduli of rocks predicted by the Kuster—Toksöz and Mori—Tanaka models. J. Geophys. Eng. 18 (4), 539–557. https://doi.org/10.1093/jge/gxab034.
- Warpinski, N.R., Mayerhofer, M.J., Vincent, M.C., Cipolla, C.L., Lolon, E., 2009. Stimulating unconventional reservoirs: maximizing network growth while optimizing fracture conductivity. J. Can. Petrol. Technol. 48 (10), 39–51. https://doi.org/10.2118/114173-pa.
- Wu, Y., Li, Y., Luo, S., Lu, M., Zhou, N., Wang, D., Zhang, G., 2020. Multiscale elastic anisotropy of a shale characterized by cross-scale big data nanoindentation. Int. J. Rock Mech. Min. Sci. 134, 104458. https://doi.org/10.1016/ j.ijrmms.2020.104458.

- Xiang, D., Chen, Z., Yang, Z., Wang, S., Deng, Y., Wang, Q., Hou, D., Zhang, G., 2017. Probing the mechanical properties of shales by nanoindentation. Geotechnical Frontiers 497–507.
- Xiong, F., Jiang, Z., Chen, J., Wang, X., Huang, Z., Liu, G., Chen, F., Li, Y., Chen, L., Zhang, L., 2016. The role of the residual bitumen in the gas storage capacity of mature lacustrine shale: a case study of the Triassic Yanchang shale, Ordos Basin, China. Mar. Petrol. Geol. 69, 205–215. https://doi.org/10.1016/ j.marpetgeo.2015.10.022.
- Yang, H., Luo, S., Zhang, G., Song, J., 2017. Elasticity of clay shale characterized by nanoindentation. ARMA US Rock Mechanics/Geomechanics Symposium. ARMA-2017-0838.
- Yang, Z., Wang, L., Zhang, G., Ho, C., 2016. Micromechanical characterization of fluidshale interactions via nanoindentation. In: SPE Asia Pacific Hydraulic Fracturing Conference. https://doi.org/10.2118/181833-MS.
- Ye, Y., Tang, S., Xi, Z., 2020. Brittleness evaluation in shale gas reservoirs and its influence on fracability. Energies 13 (2), 388. https://doi.org/10.3390/ en13020388.
- Yin, L., Yin, X., Zong, Z., 2020. A new rock physics model of shale on the theory of micro-nano pores. In: EAGE 2020 Annual Conference & Exhibition Online. https://doi.org/10.3997/2214-4609.202010308.
- Yoon, H., Ingraham, M.D., Grigg, J., Rosandick, B., Mozley, P., Rinehart, A., Mook, W.M., Dewers, T., 2019. Impact of Depositional and Diagenetic Heterogeneity on Multiscale Mechanical Behavior of Mancos Shale, New Mexico and Utah, USA. https://doi.org/10.1306/13672214M1213824.
- Zargari, S., Prasad, M., Mba, K.C., Mattson, E.D., 2011. Organic maturity, hydrous pyrolysis and elastic property in shales. In: SPE Canada Unconventional Resources Conference. https://doi.org/10.2118/149403-MS.
- Zhang, Y., Li, T., Xie, L., Yang, Z., Li, R., 2017. Shale lamina thickness study based on micro-scale image processing of thin sections. Gas Science and Engineering 46, 817–829. https://doi.org/10.1016/j.jngse.2017.08.023.
- Zhao, J., Jin, Z., Hu, Q., Liu, K., Jin, Z., Hu, Z., Nie, H., Du, W., Yan, C., Wang, R., 2018. Mineral composition and seal condition implicated in pore structure development of organic-rich Longmaxi shales, Sichuan Basin, China. Mar. Petrol. Geol. 98, 507–522. https://doi.org/10.1016/j.marpetgeo.2018.09.009.
- Zhao, J., Zhang, D., Wu, T., Tang, H., Xuan, Q., Jiang, Z., Dai, C., 2019. Multiscale approach for mechanical characterization of organic-rich shale and its application. Int. J. GeoMech. 19 (1), 04018180. https://doi.org/10.1061/(ASCE) GM.1943-5622.0001281.
- Zhao, J., Zhang, W., Zhang, D., Wei, R., Wang, Y., 2020. Influence of geochemical features on the mechanical properties of organic matter in shale. J. Geophys. Res. Solid Earth 125 (9), e2020JB019809. https://doi.org/10.1029/2020jb019809.
- Zhong, Z., Meguid, S., 1997. On the elastic field of a shpherical inhomogeneity with an imperfectly bonded interface. J. Elasticity 46, 91–113. https://doi.org/10.1023/A:1007342605107.
- Zhu, W., Hughes, J.J., Bicanic, N., Pearce, C., 2007. Nanoindentation mapping of mechanical properties of cement paste and natural rocks. Mater. Char. 58 (11–12), 1189–1198. https://doi.org/10.1016/j.matchar.2007.05.018.
- Zimmerman, R., 1984. Elastic moduli of a solid with spherical pores: new self-consistent method. Int. J. Rock Mech. Min. Sci. Geomech. Abstracts 339–343. https://doi.org/10.1016/0148-9062(84)90366-8.